Cloud-convection Feedback in Brown Dwarf Atmospheres

Maxence Lefèvre[1] , Xianyu Tan[1] , Elspeth K. H. Lee[2] , and R. T. Pierrehumbert[1]
[1] Department of Physics (Atmospheric, Oceanic and Planetary Physics), University of Oxford, Parks Road, Oxford, OX1 3PU, UK
maxence.lefevre@physics.ox.ac.uk
[2] Center for Space and Habitability, University of Bern, Gesellschaftsstrasse 6, CH-3012 Bern, Switzerland

Abstract

Numerous observational evidence has suggested the presence of active meteorology in the atmospheres of brown dwarfs. A near-infrared brightness variability has been observed. Clouds have a major role in shaping the thermal structure and spectral properties of these atmospheres. The mechanism of such variability is still unclear, and neither 1D nor global circulation models can fully study this topic due to resolution. In this study, a convective-resolving model is coupled to gray-band radiative transfer in order to study the coupling between the convective atmosphere and the variability of clouds over a large temperature range with a domain of several hundred kilometers. Six types of clouds are considered, with microphysics including settling. The clouds are radiatively active through the Rosseland mean coefficient. Radiative cloud feedback can drive spontaneous atmospheric variability in both temperature and cloud structure, as modeled for the first time in three dimensions. Silicate clouds have the most effect on the thermal structure with the generation of a secondary convective layer in some cases, depending on the assumed particle size. Iron and aluminum clouds also have a substantial impact on the atmosphere. Thermal spectra were computed, and we find the strongest effect of the clouds is the smoothing of spectral features at optical wavelengths. Compared to observed L and T dwarfs on the color–magnitude diagram, the simulated atmospheres are redder for most of the cases. Simulations with the presence of cloud holes are closer to observations.

1. Introduction

Since the first two confirmations of the observations of brown dwarfs (Nakajima et al. 1995; Rebolo et al. 1996), about 2000 similar objects have been observed, the vast majority of them free floating. These objects are classified into three types: L, T and Y dwarfs in decreasing temperature range. The L dwarfs are cooler than the M dwarf but exhibit similarities in photospheric chemical composition, containing alkali lines (K, Na), metal hybrids (FeH), oxides (TiO, VO), and water. The so-called L/T transition occurs at effective temperatures around 1100–1400 K. The L dwarfs appear redder in the color–magnitude diagram, with CO absorption, while T dwarfs appear bluer with stronger CH_4 absorption features (Kirkpatrick 2005; Cushing 2014). The chemical change is attributed to the cooling of the atmosphere. The L/T transition is presumably linked to the formation of iron and silicate clouds in the photosphere of L dwarfs, shifting them redder in the color–magnitude diagram (Tsuji et al. 1996; Ackerman & Marley 2001; Allard et al. 2001; Burrows et al. 2006). The Y dwarfs are colder and show H_2O and CH_4 absorption bands in the near-infrared, as well as water cloud features (Morley et al. 2014).

The variability of the light curve in the IR is thought to be caused by inhomogeneous surface brightness due to rotational modulation (Radigan et al. 2012; Apai et al. 2013; Karalidi et al. 2016), evolving over a few rotation periods (Artigau et al. 2009; Radigan et al. 2012; Biller et al. 2013; Gillon et al. 2013; Metchev et al. 2015; Apai et al. 2017), suggesting a rapid change of the surface features. The horizontal variation of the cloud and temperature structure (Radigan et al. 2012; Apai et al. 2013; Buenzli et al. 2015; Karalidi et al. 2016) could also play a role in this variability, but the mechanisms controlling clouds dynamics are still under investigation.

The effect of clouds has been studied using 1D radiative–convective models, with sophisticated models computing the cloud self-consistently with microphysics and parametric cloud models using fixed parameters to describe the cloud particle distribution. For the first category, there is the model Drift-Phoenix (Helling et al. 2008; Witte et al. 2009) with a full microphysics scheme with cloud formation on TiO_2; Gao et al. (2018) with condensation of KCl clouds; BT-Settl (Allard et al. 2012), which includes 40 condensable species; Exo-REM (Charnay et al. 2018) using iron, silicate, and sulfide and alkali salt clouds and Tan & Showman (2019) using $MgSiO_3$ clouds. For the second category, there is Tsuji (2002), who include corundum, iron, and silicate clouds; Ackerman & Marley (2001), Marley et al. (2010), and Morley et al. (2012, 2014) who include iron, silicate, sulfide, salt, and water clouds; and Burrows et al. (2006) and Madhusudhan et al. (2011), who include iron and silicate clouds.

The dynamics of such objects have been studied with global circulation models (GCMs): Showman & Kaspi (2013) presented the first global models of interior convection, showing the importance of rotation in the dynamics. Zhang & Ahowman (2014) performed global simulations using a one-and-a-half layer shallow-water model. Tan & Showman (2017) studied the effect of latent heating associated with condensation of silicates and iron on the dynamical circulation using an idealized 3D GCM. Showman et al. (2019) parameterized interactions between convection and the stratified layers as isotropic, stochastic temperature perturbations in the GCM and

explored their effect on zonal jet formation. Tan & Showman (2021a, 2021b) studied the effects of enstatite cloud radiative feedback on global circulation. Several models studied the dynamics of irradiated brown dwarfs (Lee et al. 2020; Tan & Showman 2020).

The GCM and 1D model have in common that they do not resolve turbulence and therefore need to use parameterization for the convective activity. The vertical transport is represented by the vertical eddy diffusivity coefficient K_{zz} that varies depending on the hypothesis (Zhang 2020). Very few studies have been conducted using a local nonhydrostatic approach, resolving the turbulence and thus not needing the K_{zz} coefficient. Freytag et al. (2010) using a 2D fully compressible equations modeled Mg_2SiO_4 clouds for temperatures between 900 and 2800 K, founding that convectively excited gravity waves are important for vertical mixing in the atmospheres. Bordwell et al. (2018) performed both 2D and 3D local fully compressible simulations studying the turbulent mixing of CO and NH_3 vapor without clouds. A new scale height was developed, derived from the chemical scale height, to predict quench points and perform 1D chemical kinetics modeling. Tremblin et al. (2021) studied radiative Rayleigh–Taylor instabilities that could influence the cloud cover.

In this study, we use a 3D local nonhydrostatic dynamical core coupled to a gray-band radiative transfer and an idealized microphysical scheme to study the vertical turbulent mixing and its impact on the convective layer for hot brown dwarfs for different cloud compositions and compare the results with 1D modeling and observations.

The paper is organized as follows. Our Cloud Resolving Model (CRM) is described in Section 2. In Section 3, the clear-sky simulations are presented, and the impact of clouds on the emission spectra is discussed in Sections 4. Our conclusions are summarized in Section 6.

2. Model Description

2.1. Dynamical Core

The CRM is using the nonhydrostatic, compressible dynamical core CM1 version 19 (Bryan & Fritsch 2002) in Large-Eddy Simulation mode. The conservation of mass, momentum, and entropy is ensured by an explicitly conservative flux-form formulation of the fundamental equations, based on mass-coupled meteorological variables (winds and potential temperature) using third-order Runge–Kutta time differencing and a fifth-order spatial derivative. A subgrid-scale prognostic turbulent kinetic energy closure (Deardorff 1980) is used to parameterize the turbulent mixing by unresolved small-scale eddies, following the strategy adopted by Kang & Bryan (2011), Wang (2014), Markowski & Bryan (2016), and Shi et al. (2018). This study is the first one to apply the CM1 dynamical core to a hydrogen atmosphere and the second applications of non-Earth atmosphere (Tan et al. 2021).

2.2. Radiative Transfer

The radiative transfer used in this study is a plane-parallel, two-stream approximation, with a gray atmosphere with a single broad thermal band for simplicity and computational efficiency. The radiative-transfer equations are solved using the numerical package TWOSTR (Kylling et al. 1995). Absorbing, emitting, and multiple-scattering atmospheres are taken into account. A frequency-averaged gas opacity is used for the

background model atmosphere, the Rosseland mean opacity $\kappa_{R,g}$ from Freedman et al. (2014) for 12 species (CH_4, CO, CO_2, CrH, FeH, H_2O, H_2S, H_2, NH_3, PH_3, TiO, and VO), and H_2 Collision Induced Absorption (CIA), over a range of metallicities (for mass fraction between 0 and 1.7). The interactions of cloud particles with radiation by absorption and scattering are parameterized by an extinction coefficient Q_{ext}, a scattering coefficient Q_{scat}, and an asymmetry parameter g. The total cloud extinction opacity $\kappa_{R,ext}$ is averaged over the wavelength:

$$\frac{1}{\kappa_{R,ext}} = \frac{\int_0^\infty \frac{1}{\kappa_{ext}(\lambda)} \frac{dB_\lambda}{dT} \, d\lambda}{\int_0^\infty \frac{dB_\lambda}{dT} \, d\lambda}, \tag{1}$$

where B_λ is the Planck function and $\kappa_{ext}(\lambda) = \int_{r_{min}}^\infty n(r)\pi r^2 Q_{ext}(r, \lambda) \, dr$ is the total cloud opacity at λ over all particle sizes (between 0.01 and 100 μm). The total opacity is the sum of gas and cloud opacity, $\kappa = \kappa_{R,g} + \kappa_{R,ext}$.

To produce the precalculated cloud opacity tables, the wavelength-dependent extinction coefficient, $Q_{ext}(r, \lambda)$; single-scattering albedo, $\omega(r, \lambda)$; and asymmetry factor, $g(r, \lambda)$ of each of our considered cloud species are calculated using the MIEX Mie code of Wolf & Voshchinnikov (2004) assuming spherical particles. A 2D grid of particle size and temperature-dependent Rosseland-weighted quantities is generated using these wavelength-dependent quantities that are able to be interpolated inside the simulation to find the cloud properties for feedback into the radiative transfer (RT) scheme. Real and imaginary optical constants for each of the cloud species are taken from Kitzmann & Heng (2018). The temperature–wavelength variation of the extinction and scattering coefficient and asymmetry factor for the six cloud compositions considered are visible in Appendix A.

2.3. Cloud Microphysical Model

The transport of condensable gas particles is represented by two tracers, one for the gas phase and one for the condensed phase. The condensation of the particles is performed as follows:

$$\frac{dq_v}{dt} = -\frac{q_v - q_s}{\tau_c}\delta + \frac{\min(q_s - q_v, q_c)}{\tau_c}(1 - \delta) + Q_{deep}, \tag{2}$$

$$\frac{dq_c}{dt} = \frac{q_v - q_s}{\tau_c}\delta - \frac{\min(q_s - q_v, q_c)}{\tau_c}(1 - \delta) + \frac{1}{\rho}\frac{\partial(\rho \langle q_c V_s \rangle)}{\delta z}, \tag{3}$$

with q_v the mass ratio of condensable vapor (kg kg^{-1}), q_c the mixing ratio of condensates (kg kg^{-1}), q_s the local saturation vapor-mixing ratio, V_s the settling speed of particles described in Equation (11), ρ the gas density, and τ_c the timescale for conversion due to condensation or evaporation. The term $Q_{deep} = -(q_v - q_{deep})/\tau_{deep}$ only applies to pressure greater than 50 bar, relaxing the local vapor q_v to the deep mixing ratio q_{deep} over a characteristic timescale τ_{deep} set to 10^3 s. A sensitivity study of τ_{deep} was conducted in Tan & Showman (2019) over three orders of magnitude with no substantial difference. The conversion timescale τ_c is set to 10 s (Helling & Casewell 2014), short compared to cloud-settling and radiative

timescales. This conversion timescale will affect the depth of the convective layer; a larger value will allow vapor or condensate that should change phase to enrich the layer that the advecting plume is in. Tests with values of 1 and 100 s were conducted; a small change in the cloud-layer depth was observed.

This study is focused on brown dwarfs with type L and T clouds. In this temperature range we considered four representative clouds that could be affected by convective activity: enstatite, iron, perovskite, and corundum. Enstatite ($MgSiO_3$) is set to represent the silicate cloud, one of the most abundant condensates in L and T dwarfs. The total gas pressure P_T(bar) at which enstatite saturates as a function of temperature T and metallicity ([Fe/H]) is calculated as follows (Visscher et al. 2010):

$$10^4/T = 6.26 - 0.35 \log(P_T) - 0.70 \, [\text{Fe/H}]. \qquad (4)$$

For the iron clouds, the equilibrium condensation temperature is set as (Visscher et al. 2010)

$$10^4/T = 5.44 - 0.48 \log(P_T) - 0.48 \, [\text{Fe/H}]. \qquad (5)$$

To represent the Ti clouds, perovskite ($CaTiO_3$) is considered, defined as (Wakeford et al. 2017)

$$10^4/T = 5.125 - 0.277 \log(P_T) - 0.554 \, [\text{Fe/H}]. \qquad (6)$$

Corundum (Al_2O_3) is representing Al clouds (Wakeford et al. 2017)

$$\begin{aligned} 10^4/T = 5.014 &- 0.2179 \log(P_T) + 2.264 \; 10^{-3} \\ &\times (\log(P_T))^2 - 0.585 \, [\text{Fe/H}]. \end{aligned} \qquad (7)$$

For the chrome clouds, the equilibrium condensation temperature is set as (Morley et al. 2012)

$$10^4/T = 6.576 - 0.486 \log(P_T) - 0.486 \, [\text{Fe/H}]. \qquad (8)$$

Alabandite (MnS) is considered (Morley et al. 2012):

$$10^4/T = 7.447 - 0.42 \log(P_T) - 0.84 \, [\text{Fe/H}]. \qquad (9)$$

The saturation mixing ratio q_s is then obtained as $q_s = P_T q_{\text{deep}}/p$. The deep mixing ratio q_{deep} relative to H and He_2 in solar abundance is set to 0.0026, 0.0012, $8.6 \; 10^{-6}$, $2.2 \; 10^{-4}$, $1.76 \; 10^{-5}$, and $2.1 \; 10^{-5}$ using, respectively, the molar fraction of Mg, Fe, Ca, Al, Cr and Mn for a solar metallicity (Lodders 2003).

In the present study, only one cloud species is included in each simulation, while in reality, multiple species of clouds may exist at the same location at a given time. For simplicity, we only examine simulations including one species at a time. This may be a reasonable approximation in circumstances when one species dominates in opacity, and it allows us to identify the behavior of each species independently. Convection coupled to more comprehensive cloud models will be studied in future work, as some species may form in the same locations simultaneously, and the properties of the most massive/thickest clouds would most likely dominate.

The release of latent heat for the different cloud particles is not taken into account. In the temperature range of the atmosphere of this study and solar metallicity, the energy from the latent heat is several orders of magnitude lower than in the Earth moist tropics (Zhang 2020). With a GCM, Tan & Showman (2017) studied the effect of silicate latent heat and found that temperature perturbations from significant silicate condensation were on the order of only 1 K.

The cloud particle number per dry airmass N_c is assumed constant throughout the atmospheric column; the local cloud properties are then determined from this number. A log-normal particle size distribution is implemented in the models, extensively used to parameterize clouds in brown dwarf atmospheres (Ackerman & Marley 2001; Barman et al. 2011; Morley et al. 2012):

$$n(r) = \frac{N_c}{\sqrt{2\pi}\,\sigma r} \exp\left(-\left(\frac{ln(r/r_0)}{\sigma}\right)^2\right), \qquad (10)$$

where r is the particle radius, $n(r)=dN_c/dr$ is the number density distribution, r_0 is the reference radius, and σ is the nondimensionalized constant measuring the width of the distribution. The parameter σ controlling the width of the size distribution is not constrained. In this study, σ is set to 1, Tan & Showman (2019) test the sensitivity to this parameter for values from 0.1 to 1.5 and found significant differences as the reference radius is changed. The reference radius r_0 is calculated by solving $q_c = \frac{4}{3}\pi\rho_c \int_0^\infty r^3 n(r)\, dr = \frac{4}{3}\pi\rho_c N_c r_0^3 \exp(-\frac{9}{2}\sigma^2)$. A maximum radius is set to 100 μm, and a minimum radius is set to 0.01 μm (Tsuji 2002).

Cloud particles of radius a are assumed to immediately reach their terminal fall speed as given by Pruppacher & Klett (1978):

$$V_s = \frac{2\beta a^2 g(\rho_p - \rho)}{9\eta}, \qquad (11)$$

where η is the viscosity of the gas, g is the gravitational acceleration of the planet, ρ_p is the density of the particle, and ρ the density of the atmosphere. β is the Cunningham slip that accounts for the gas kinetic effects, becoming relevant when the mean free path of the atmospheric molecules is bigger than the size of the falling particle. The expression of β determined from experiments (Li & Wang 2003) is

$$\beta = 1 + K_N(1.256 + 0.4e^{(-1.1/K_N)}), \qquad (12)$$

where K_N is the Knudsen number, the ratio of the mean free path λ to the size of the particle a, $K_N = \lambda/a$. For a perfect gas, the mean free path can be expressed as (Chapman & Cowling 1970)

$$\lambda = \frac{k_B T}{\sqrt{2}\,\pi d^2}\frac{1}{P}; \qquad (13)$$

for the viscosity η of hydrogen, the analytical formula from Rosner (1986) is used

$$\eta = \frac{5}{16}\frac{\sqrt{\pi m k_B T}}{\pi d^2}\frac{(k_B T/\epsilon)^{0.16}}{1.22} \qquad (14)$$

with d the molecular diameter, m the molecular mass, and ϵ the depth of the Lennard–Jones potential well. m is set to 2.827×10^{-10} m and ϵ to $59.7 k_B$ K. This expression is valid for temperatures between 300 and 3000 K and for pressures less than 100 bar (Stiel & Thodos 1963).

2.4. Simulation Settings

Figure 1 shows the initial temperature profiles from the Tan & Showman (2019) model and the condensation curve for the different cloud species considered. The horizontal resolution is 2 km between 200 and 360 points, depending on the temperature case. The vertical domain extends from $3 \, 10^7$ to 10^4 Pa for the lowest surface temperature case and $3 \, 10^3$ Pa for
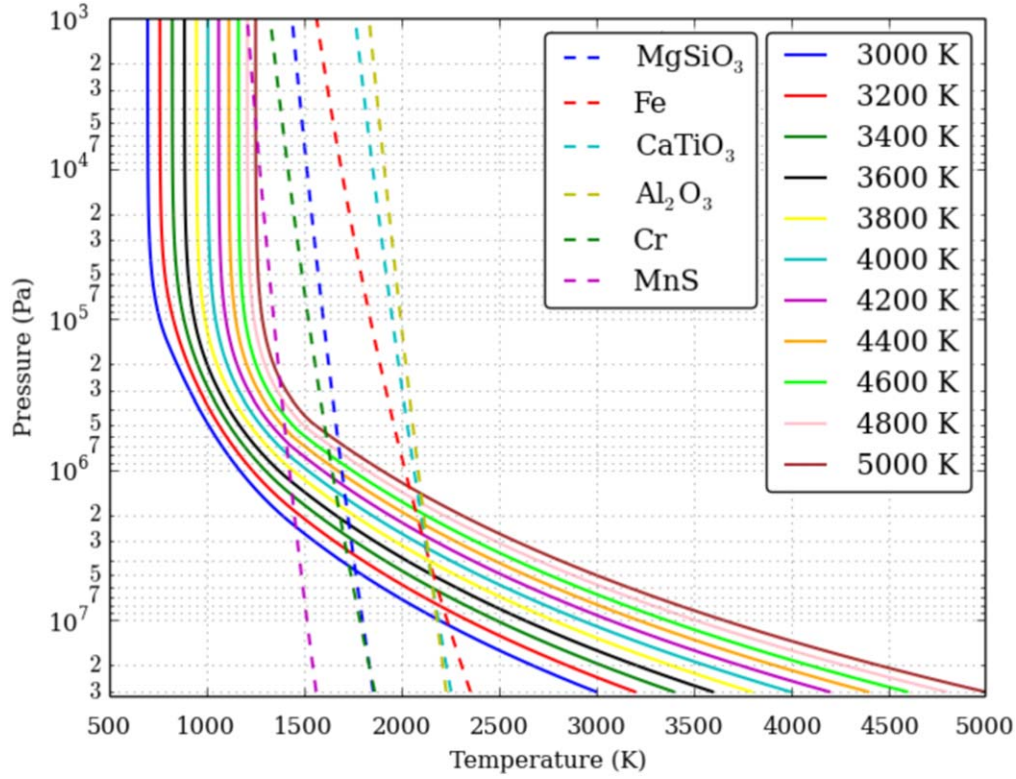
Figure 1. Initial vertical temperature profile (solid line) and condensation profile for the considered clouds (dotted line). The effective temperatures are for the clear-sky cases.

Table 1
Planetary and Atmospheric Parameters for the Different Simulations

Parameter	Value				
Gravity (m s^{-2})	1000				
Heat capacity (J K^{-1})	13,000				
Surface pressure (Pa)	3×10^7				
Mean molecular mass (g mol^{-1})	2.23				
Cloud composition	MgSiO$_3$,	Fe,	CaTiO$_3$,	Al$_2$O$_3$,	Cr, MnS
Deep mixing ratio (kg kg^{-1})	2.6 10^{-3},	1.2 10^{-3},	8.6 10^{-6},	2.2 10^{-4},	1.76 10^{-5} 2.1 10^{-5}
Horizontal resolution (km)	2				

Surface temperature (K)	Effective temperature (K)	Domain
3000	860	$200 \times 200 \times 200$
3200	940	$200 \times 200 \times 200$
3400	1010	$240 \times 240 \times 200$
3600	1090	$280 \times 280 \times 250$
3800	1160	$280 \times 280 \times 260$
4000	1230	$280 \times 280 \times 270$
4200	1290	$280 \times 280 \times 270$
4400	1350	$300 \times 300 \times 270$
4600	1400	$300 \times 300 \times 280$
4800	1450	$320 \times 320 \times 300$
5000	1500	$360 \times 360 \times 300$

the highest. The time step is 0.5 s. To avoid the spurious reflection of upward-propagating gravity waves on the model top, a Rayleigh damping layer where the energy is dissipated is applied over the 10 last levels with a damping coefficient of $1/3\ 10{-}2$ s^{-1}. The surface is set constant in space and time. We evaluate results after simulating 24 hr of time in cloudless cases, and 48 hr of time for cloudy cases. The vapor tracer is set at the start of the simulation at the deep mixing ratio on the first level,

and the cloud tracer is set to zero. The vapor tracer is then advected vertically by the convection and condensates when it is possible. The different parameters are summarized in Table 1.

3. Cloud-free Atmosphere

Figure 2 displays the domain-averaged vertical profiles of the potential temperature (left) and IR heating rates (right) for
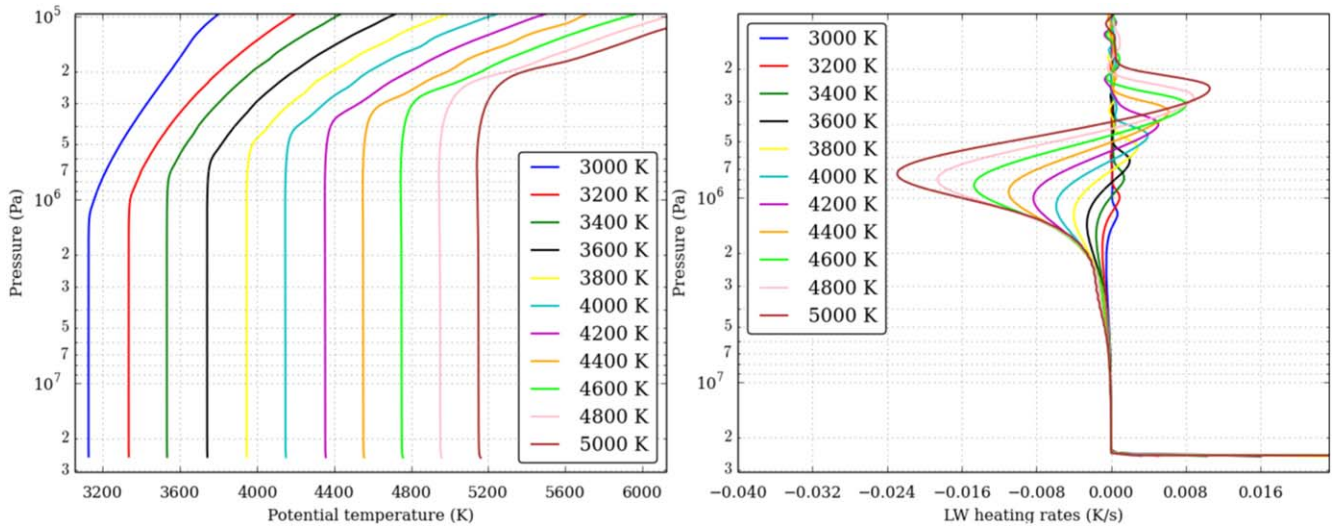
Figure 2. Domain-averaged vertical profiles of the potential temperature (left) and IR heating rates (right) for the clear-sky cases.

10 different temperature cases, all cloud free for a solar-metallicity value. The potential temperature is calculated using the heat capacity, and the surface pressure in Table 1 is the reference pressure. The depth of the convective layer is visible in the constant value of the potential temperature, following a straightforward behavior: The thickening of the convective layer is expected from the increase in opacity that comes with increasing temperature (Pierrehumbert 2010). This is what is observed in the right panel of Figure 2. Using a hydrostatic formulation, the depth of the convective layer in kilometers is comparable to the one in Freytag et al. (2010). Positive heating rates above 10^6 Pa are caused by convective overshooting, which balances the excessive heating caused by convective penetration. This effect is important to determine the top of the convective zone and is usually absent in 1D models.

Figure 3 shows snapshots of the vertical (left column) and horizontal (right column) cross section of the vertical wind for three clear-sky temperature cases: 3000 K (top row), 4000 K (middle row), and 5000 K (bottom row). The temperature trend on the convection depth has an impact on the convection depth —a hotter atmosphere will exhibit higher vertical wind, with a value six times higher between the two extreme temperature cases presented here. The convective layer organizes itself on the horizontal plane with polygonal cells with a diameter that will vary in temperature, from 80 km at 3000 K to 300 km at 5000 K. The values of the decimal logarithm value of the vertical velocity rms in cm s^{-1}, 3.5 at 5.6 10^6 Pa for the 3000 K case, 3.9 at 2.7 10^6 Pa for the 4000 K, 4.2 at 2 10^6 Pa for the 5000 K case, are comparable to the Freytag et al. (2010) values with a similar temperature trend. This temperature trend is comparable to the scaling of vertical velocity with flux from mixing-length theory (Stevenson 1979).

Figure 4 displays the domain-averaged vertical profiles of the vertical eddy diffusivity for the 10 temperature cases calculated estimated as follows:

$$K_{zz} = -\frac{\overline{\theta' w'}}{\partial \overline{\theta}/\partial z},$$ (15)

with θ the potential temperature, w the vertical wind, primed quantities representing perturbations relative to the domain-averaged values, and overlined quantities representing domain-averaged values. The vertical eddy diffusivity exhibits the same temperature trend as the depth of convection, varying by a factor of 3 between the two extreme temperature cases. The vertical eddy diffusivity has been estimated using tracers instead of potential temperature, and the values are of the same order of magnitude. The convective layer value is about 10^6 m^2 s^{-1}; above, there are gravity waves participating in the diffusion but with several orders of magnitude lower than convection. This value of 10^6 m^2 s^{-1} is higher than the value obtained by Freytag et al. (2010) with convection-resolving modeling. With mixing-length theory, the estimation of the vertical eddy diffusion is comparable with that of Freytag et al. (2010). This value of the vertical eddy diffusivity in the convective layer is consistent with previous estimations (Lewis et al. 2010; Moses et al. 2011). In Tan & Showman (2019), with a similar thermal structure and radiative transfer, the estimated vertical eddy diffusivity at 10^6 Pa is about the same order of magnitude. The scaling with temperature of the vertical eddy diffusivity is consistent with previous estimations (Ackerman & Marley 2001). Above the convective layer, the value of the vertical eddy diffusivity drops significantly and should not be used in GCMs or 1D simulations due to the absence of wind shear and general circulation.

The Freedman et al. (2014) gas opacity formulation takes into account the metallicity of the atmosphere, and simulations of clear-sky atmosphere with several metallicities have been performed. Figure 5 shows the impact of metallicity on the convective layer depth. The solid lines are for a solar-metallicity value, similar to previous figures, and the dashed lines are for a metallicity equal to 10 times the solar metallicity. The change in convection depth is barely noticeable at low temperature, and for the high-temperature cases, the convective layer depth increases with metallicity.

4. Impact of Clouds

Figure 6 displays the domain-averaged vertical profiles of the potential temperature (left) and cloud opacity (right) for the six cloud compositions considered in this study for a cloud particle number density of 10^8 kg^{-1} per dry airmass and one
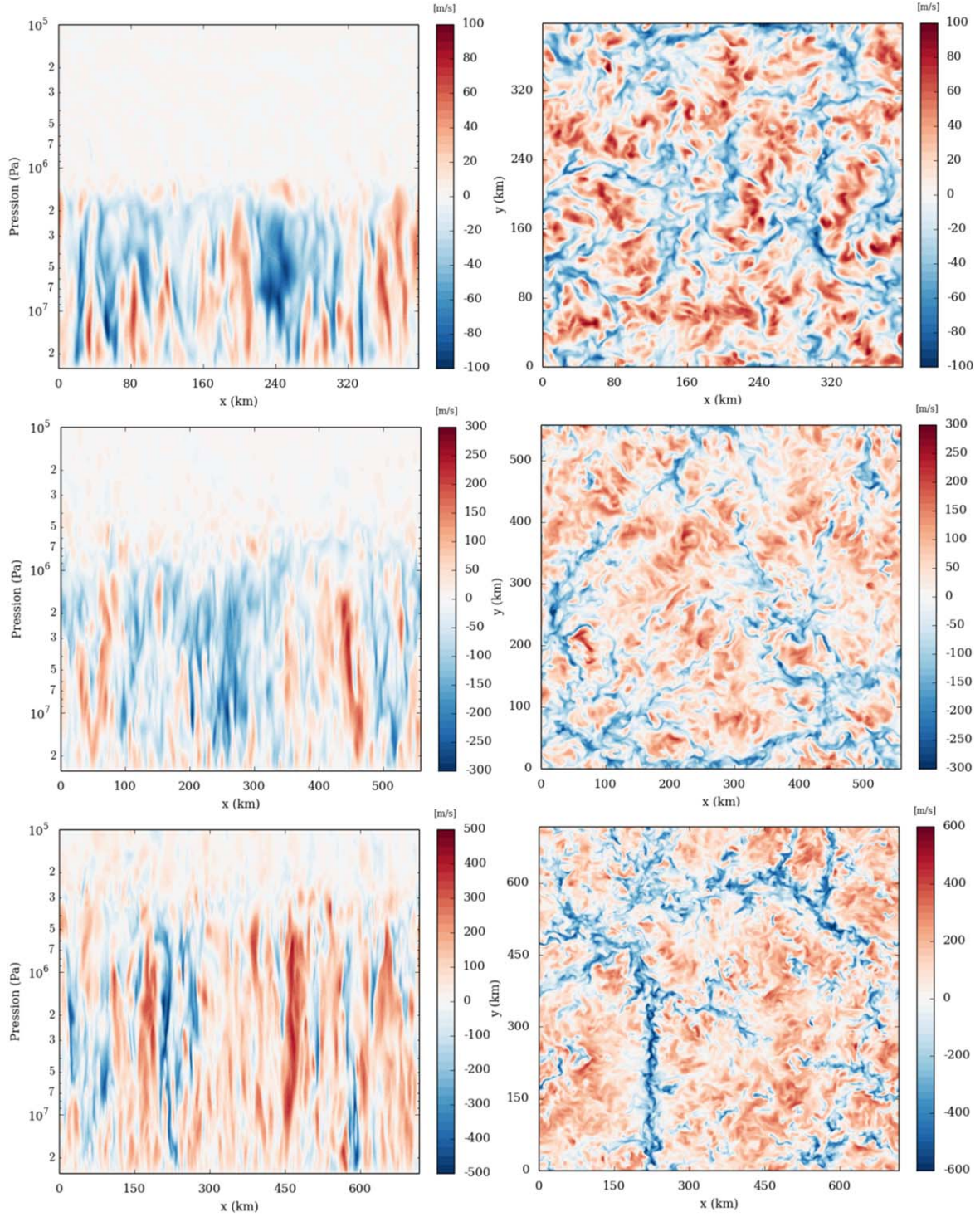
Figure 3. Snapshots of the vertical (left column) and horizontal (right column) cross section of the vertical wind for the clear-sky 3000 K case (top row), 4000 K case (middle row), and 5000 K case (bottom row). The horizontal cross section is at $5.6 \, 10^6$ Pa for the 3000 K case, at $2.7 \, 10^6$ Pa for the 4000 K case, and at $2 \, 10^6$ Pa for the 5000 K case.

temperature case. Three categories can be discerned: clouds with opacity less than 1 and no impact on the convective layer composed of $CaTiO_3$, Cr, and MnS; clouds with opacity greater than 1 and moderate impact composed of Fe and Al_22O_3; and clouds with opacity greater than 1 and high impact composed of $MgSiO_3$. A small cloud particle number per dry airmass will increase the horizontal variability and can in some cases engender cloud holes. The τ_c conversion timescale will affect the cloud-layer vertical thickness. With a larger timescale value, cloud particles will be able to mix to deeper layers before they evaporate.

4.1. MgSiO₃ Clouds

Figure 7 shows on the left column the domain-averaged vertical profiles of the potential temperature, cloud-mixing ratio, and IR heating rates for three temperatures cases with
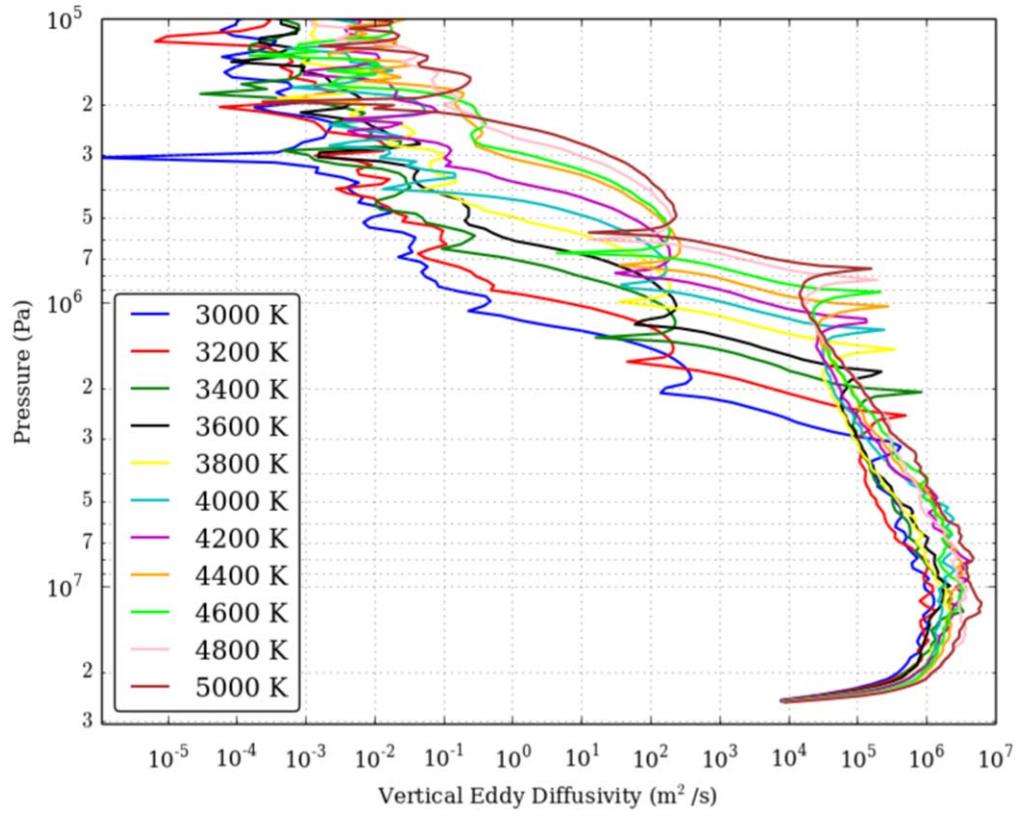
Figure 4. Domain-averaged vertical profiles of the vertical eddy diffusivity ($m^2\ s^{-1}$) for the clear-sky cases.
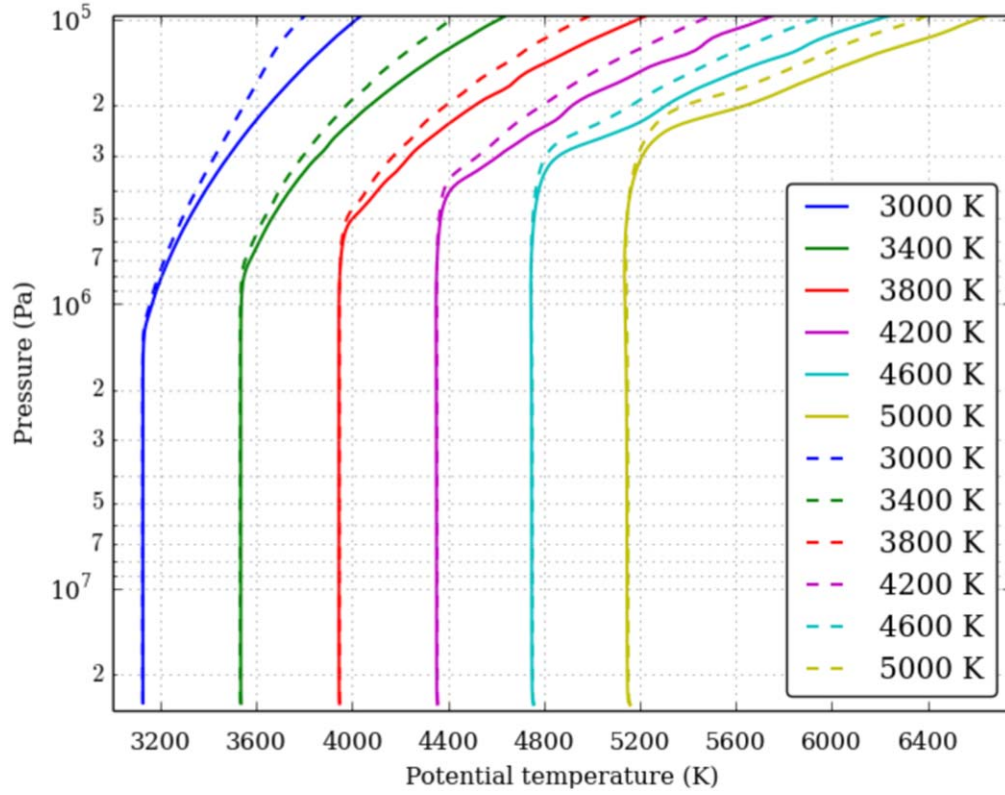

Figure 5. Domain-averaged vertical profiles of the potential temperature for solar metallicity (solid lines) and 10 times the solar metallicity (dashed lines) for six clear-sky temperature cases.
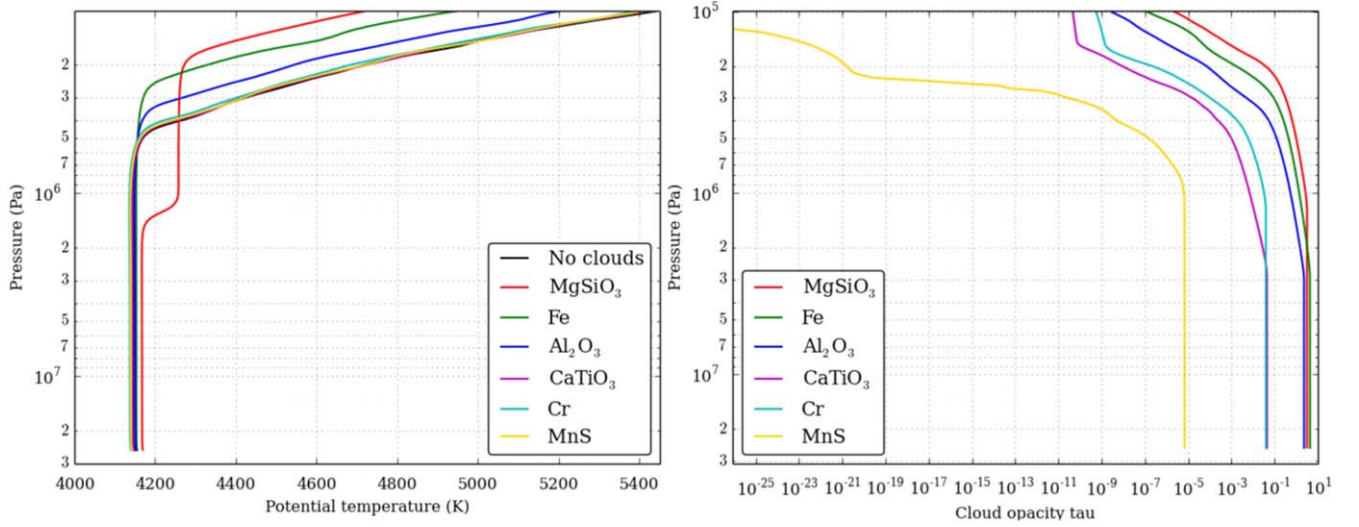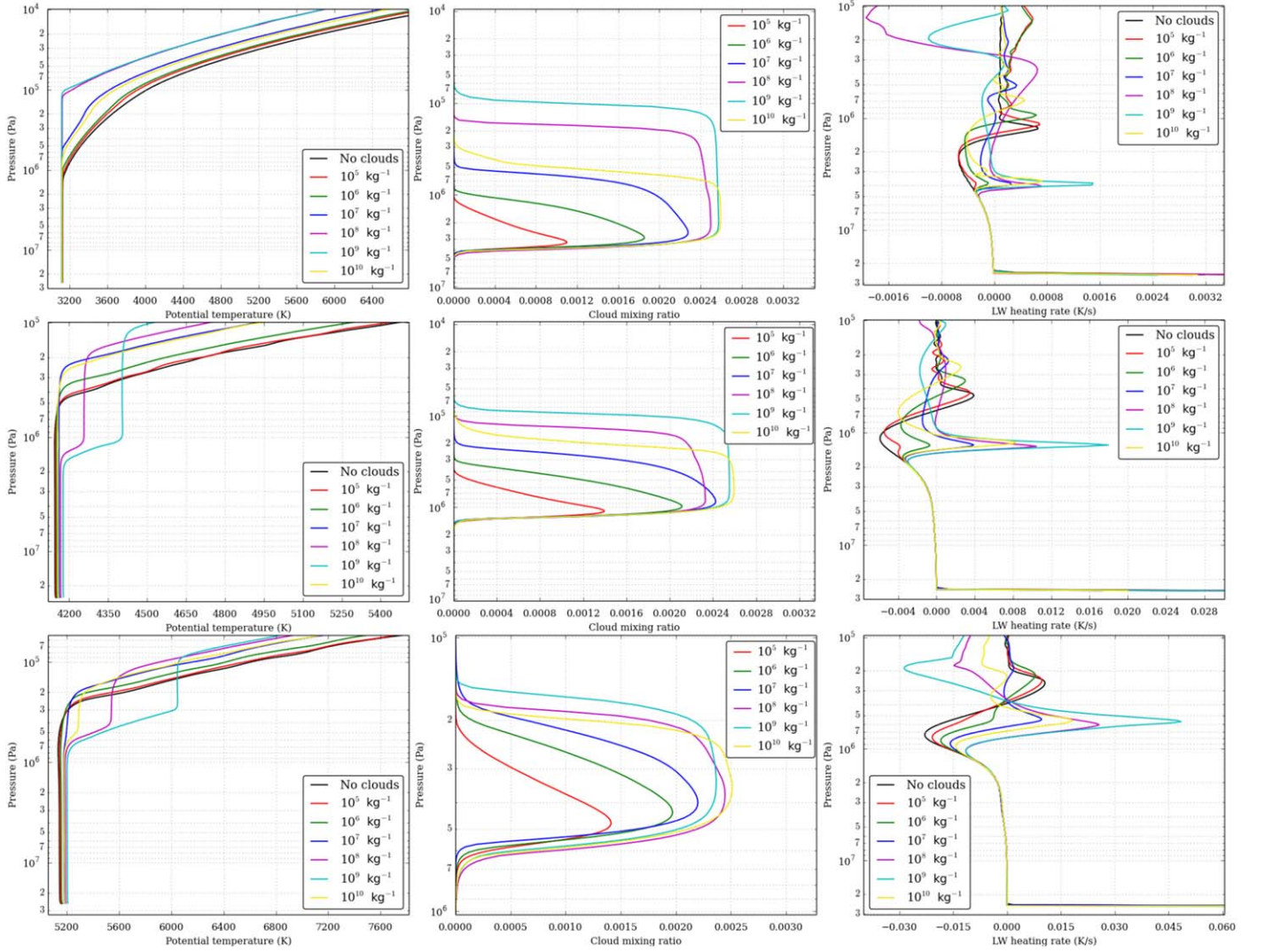
Figure 6. Domain-averaged vertical profiles of the potential temperature (left) and cloud opacity (right) for the six cloud compositions considered with a cloud particle number density of $10^8 \, \mathrm{kg}^{-1}$ for the 4000 K case.

Figure 7. Domain-averaged vertical profiles of the potential temperature (left column), cloud-mixing ratio (middle column), and IR heating rates (right column) for the 3000 K (top row), 4000 K (middle row), and 5000 K (bottom row) cases with MgSiO$_3$ clouds and particle number per dry airmass between 10^5 and $10^{10} \, \mathrm{kg}^{-1}$.

$MgSiO_3$ clouds and six different particle numbers per dry airmass values. The associated domain-averaged vertical profiles of the reference particle radius, scattering albedo, and opacity are visible in Appendix B, Figure 22.

The depth of the convective layer is strongly affected by the presence of $MgSiO_3$ clouds, with a strong increase of the top boundary of the convection. The presence of clouds is visible in the IR heating rate with a strong clouds-induced heating at 4×10^6 Pa for the 3000 K case, 1.5×10^6 Pa for the 4000 K case, and at 6×10^5 Pa. This increase is different for the five different particle number per dry airmass values considered. For the low values, 10^5 and $10^6\,kg^{-1}$, the cloud particle reference radius is larger, above $10\,\mu m$, resulting in small opacities and small scattering albedo and therefore to a limited impact on the atmosphere. The IR heating vertical profiles are hardly changed for the three temperature cases shown here. The two cases of 10^7 and $1e^{10}\,kg^{-1}$ particle number per dry airmass have a similar impact on the convection depth, despite a difference in radii. The $1e^7\,kg^{-1}$ case leads to a reference radius around $5\,\mu m$, resulting in cloud particles with small opacities but high scattering albedo. Whereas the $1e^{10}$ case leads to a small reference radius around $0.5\,\mu m$, resulting in small scattering albedo but higher opacities. The overall increase on the convection depth is similar. Finally, the 10^7 and $10e^{10}\,kg^{-1}$ particle number per dry airmass cases have strong impacts. With reference radius 1 and $2.5\,\mu m$, the clouds have high opacities, greater than 1 for the three temperature cases, and high scattering albedo, up to 0.7, resulting in strong heating. This heating leads in some cases to a detached convective layer, a secondary convective layer on top of the deep convective layer induced by the deep atmosphere with a different potential temperature than the deep atmosphere. This impact on the depth of the convective layer will engender a modification of the thermal structure above this layer and therefore a change in the effective temperature. For the 3000 K case, the effective temperature is equal to 860 K and drops to an average of 840 K, 830 K, 780 K, 690 K, 680 K, and 790 K for, respectively, a cloud particle number per dry airmass of $10^5\,kg^{-1}$, $10^6\,kg^{-1}$, $10^7\,kg^{-1}$, $10^8\,kg^{-1}$, $10^9\,kg^{-1}$, and $10^{10}\,kg^{-1}$. For the 4000 K case, the effective temperature is equal to 1230 K and drops to an average of an average of 1170 K, 1190 K, 1080 K, 1050 K, 990 K, and 1090 K for, respectively, a cloud particle number per dry airmass of $10^5\,kg^{-1}$, $10^6\,kg^{-1}$, $10^7\,kg^{-1}$, $10^8\,kg^{-1}$, $10^9\,kg^{-1}$, and $10^{10}\,kg^{-1}$. For the 5000 K case, the effective temperature is equal to 1500 K and drops to an average of 1475 K, 1440 K, 1390 K, 1340 K, 1330 K, and 1370 K for, respectively, a cloud particle number per dry airmass of $10^5\,kg^{-1}$, $10^6\,kg^{-1}$, $10^7\,kg^{-1}$, $10^8\,kg^{-1}$, $10^9\,kg^{-1}$, and $10^{10}\,kg^{-1}$. As expected, the cases in which there is a detached convective layer are the ones with the largest temperature decrease.

Figure 8 shows snapshots of the cloud-mixing ratio for the 4000 K case with $MgSiO_3$ clouds for four different cloud particle numbers per dry airmass and associated brightness temperatures. The effect of the cloud particle number per dry airmass on the cloud is visible, the cloud tends to be more nonhomogeneous and cloud holes are visible in the $10^5\,kg^{-1}$ case (top row) but are not present for the $10^8\,kg^{-1}$ case. The $10^9\,kg^{-1}$ and $10^{10}\,kg^{-1}$ cases are not shown for clarity, but the homogenization of the cloud is stronger than that for the $10^8\,kg^{-1}$ case. With a small cloud particle number per dry airmass, the particle diameter is bigger (Figure 22), and

therefore, the terminal settling velocity will be higher by several orders of magnitude. For the low cloud particle number per dry airmass cases, it becomes significant relative to the convective vertical velocity, creating a competition between the two, resulting in cloud holes. When the bulk setting velocity is comparable to the flow vertical velocity, the settling timescale is comparable to the vertical advection timescale. Thick clouds are thus sustained only in regions of updrafts, whereas in downdraft regions clouds settle out quickly, generating significant cloud patchiness. In simulations with a much smaller bulk setting velocity, for a cloud particle number per dry airmass (below $10^7\,kg^{-1}$) higher than the flow vertical velocity, horizontal mixing effectively homogenizes the cloud structure in the domain. The effect of complete cloud coverage is also visible in the brightness temperature; with high cloud particle number values, the outgoing radiative flux is lower.

Figure 9 shows snapshots of the cloud-mixing ratio and brightness temperature for the three temperature cases with $MgSiO_3$ clouds for a $10^8\,kg^{-1}$ cloud particle number per dry airmass. In the three cases, the mixing ratio of the cloud particles are pretty uniform with noticeable cellular features. The cloud pattern changes with increasing temperature, showing some tendency to convective aggregation at high temperature. For the 3000 K case, the cloud holes are small—cells of a few tens of kilometers—whereas for the 5000 K, the cloud holes are dominated by a 400 km diameter structure. This is due to the convective structure, as shown in Figure 3 there is an increase of the convective cell diameter with increasing temperature due to the thickening of the convective layer. At low temperature, the downdraft region is narrow whereas with the increase in temperature, the downdraft region where several updrafts meet can be quite large, leading to a cloud hole with the settling velocity. At low cloud particle numbers and high temperatures, there can be large cloud holes of several hundreds of kilometers in diameter.

4.1.1. Detached Convective Layer

These detached convective layers are triggered by an intense IR heating induced by the clouds that destabilize the atmosphere and engender a separate convective layer visible on the left column of Figure 7 by an area above 10^6 Pa with a distinctive constant potential temperature. This strong cloud greenhouse effect produces a stratified layer below the cloud base, which splits the convection zone into two. The root cause behind this effect is that cloud opacity decreases rapidly with increasing pressure near the cloud base, and this configuration favors a stratified layer. In the 3000 K case, there is a detached convective layer for a particle number density of $10^8\,kg^{-1}$ that is not discernible in the figure. In the 4000 K case, the particle number density values of 10^8 and $10^9\,kg^{-1}$ generate a detached convective layer, whereas for the 5000 K case, a detached convective layer is present for the 10^8, 10^9, and $10^{10}\,kg^{-1}$ particle number density cases. Figure 10 shows instantaneous snapshots of the detached convective layer for the 4000 K case and a particle number density of $10^8\,kg^{-1}$. This cloud greenhouse effect on the detached zones has been seen in many previous 1D models with clouds (Burrows et al. 2006; Tan & Showman 2019).

The detached convective layer is visible between 10^6 and 2×10^5 Pa; below it, the deep convective layer is visible in the vertical cross section of the vertical wind. The associated horizontal cross section shows the organization of the
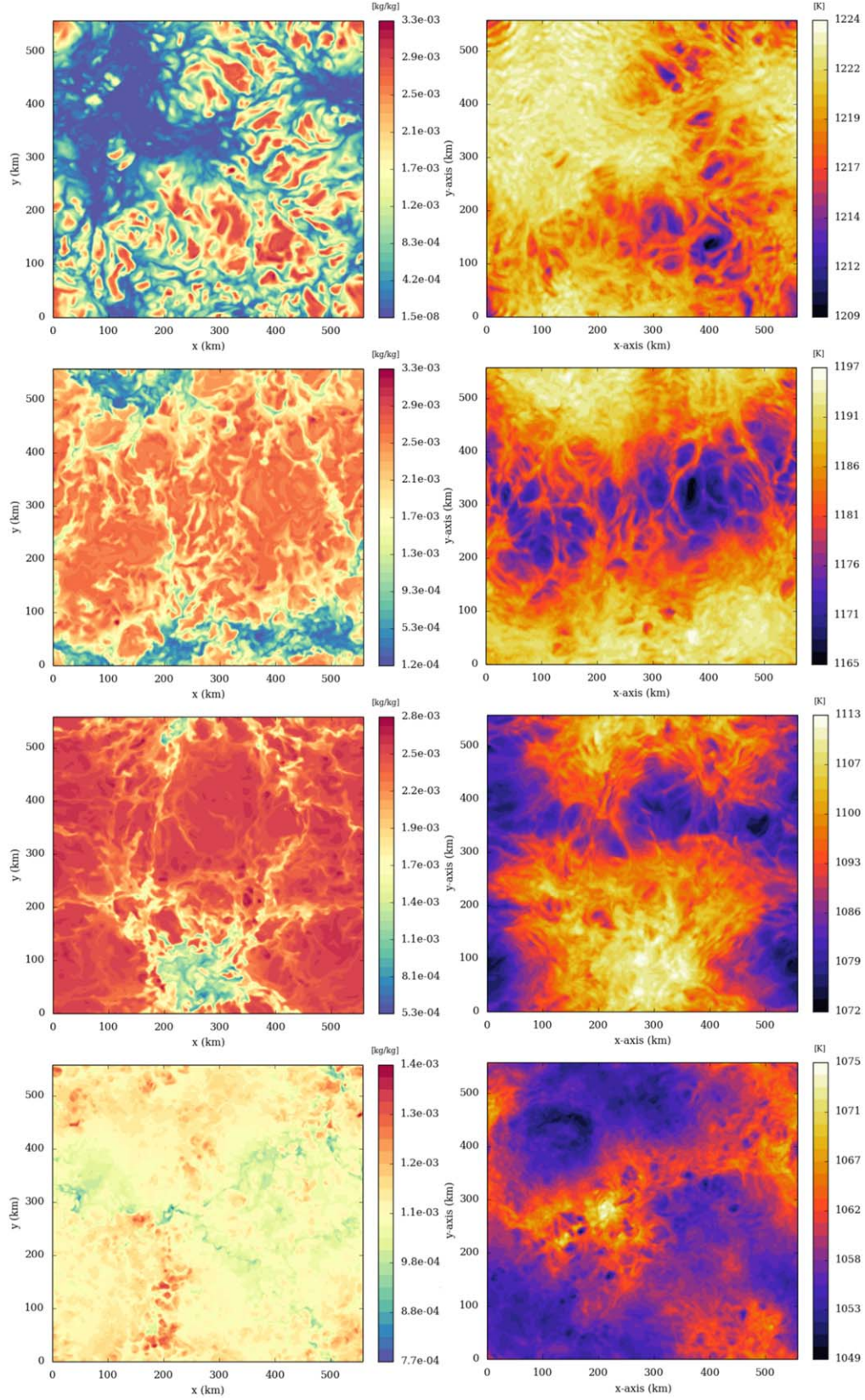
Figure 8. Snapshots of the horizontal cross section at 5.4×10^5 Pa of the cloud-mixing ratio (left column) and the brightness temperature (right column) for the 4000 K case with $MgSiO_3$ clouds and cloud particle number per dry airmass from top to bottom of 10^5, 10^6, 10^7 and 10^8 kg^{-1}.

convection. Contrary to the deep convective layer organized in closed-polygonal cells (see Figure 3), the detached convective layer is organized with weak large polygonal updrafts (see

Figure 10, top-right panel, at $x = 200$ km and $y = 450$ km) surrounded by strong small updrafts with positions varying in time (see Figure 10, top-right panel at $x = 200$ km and
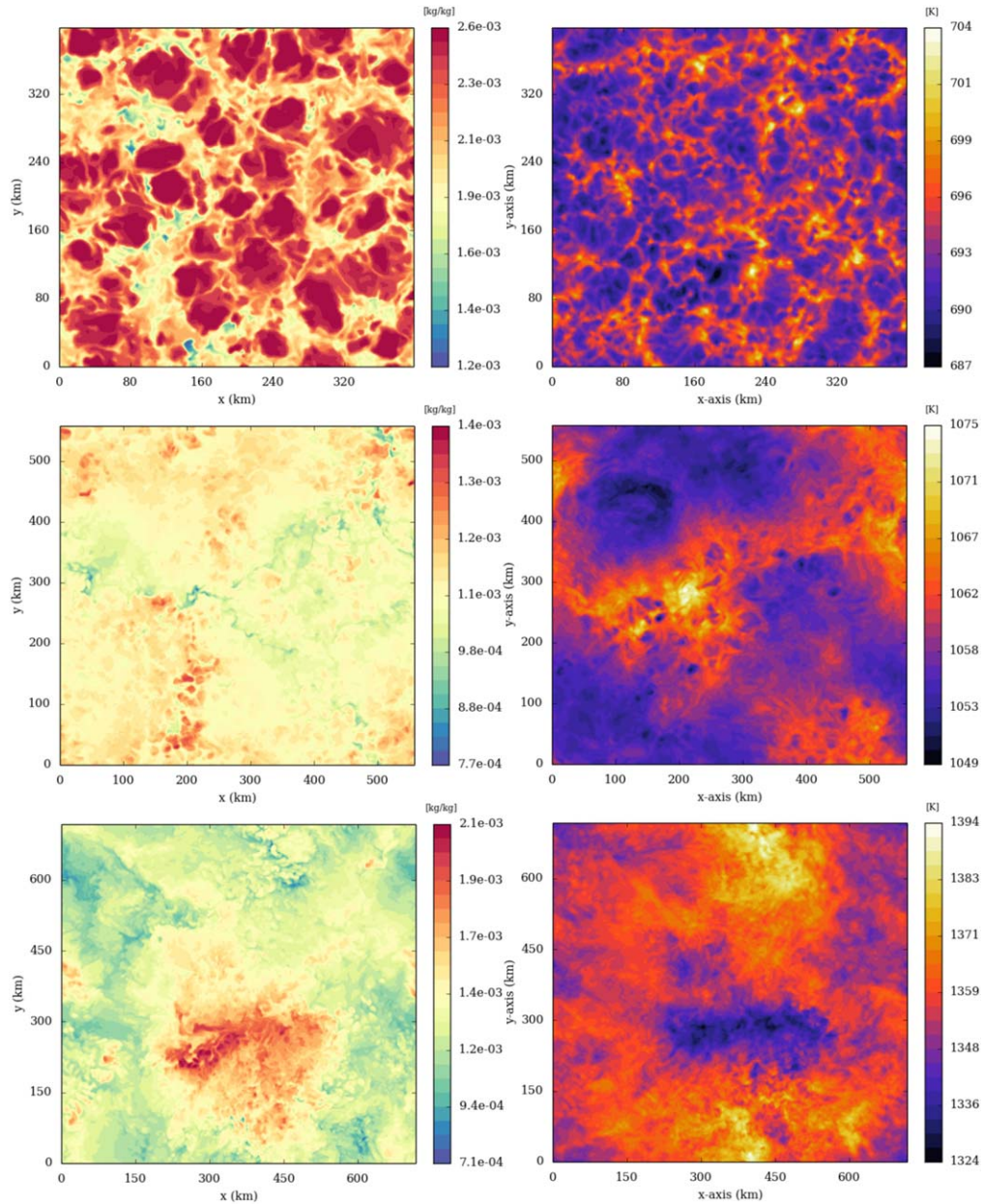
Figure 9. Snapshots of the horizontal cross section of the cloud-mixing ratio (left column) and the brightness temperature (right column) for the 3000 K case (top row), the 4000 K case (middle row), and the 5000 K case (bottom row) with $MgSiO_3$ clouds and cloud particle number per dry airmass of $10^8 \, kg^{-1}$.

$y = 300$ km). The heating due to clouds scattering at the base of this detached layer is strong enough to maintain the convective layer detached but not enough to sustain a polygonal cell organization, resulting in a puffiness of the convective updraft and clouds. The vertical eddy diffusion is lower (between 10^3 and $10^4 \, m^2 \, ^{-1}$) for the cases showed in Figure 10, lower than in the deep convective layer due to the nonhomogeneity of the convective plume strength. The position of the strong updraft region evolves in time. The height and thickness of the detached convective layer depend on the heating induced by the cloud; the stronger it is, the higher and thicker the convective layer will be. The metallicity also has an effect on the detached convective layer.

The temporal variability of this detached convective layer with a time series of vertical cross section of the vertical wind is shown in Figure 11 over 15 hr. The deep convective activity is visible below 10^6 Pa. Comparing the two convective layers,

there is a strong variability in the detached convective layer. Figure 11(b) and Figure 11(f) represent two extreme cases, where for the first one there is a tenuous convective activity with low vertical wind, and on the contrary, for the second one there is a substantial convective activity with a vertical wind similar in amplitude to the deep convection. In between those two, there are transient steps with regions without barely any convective activity and regions with significant convection. The frequency of occurrence of those convective plumes is roughly about 7–8 hr. This frequency is of the same order of magnitude as in Tan & Showman (2019), over several hours; however, the domain-mean variability on the potential temperature is lower. The impact on the clouds is also weaker—the temporal variation of the cloud abundance is inferior by one order of magnitude. This might be due to the vertical mixing inside this detached layer in the Tan & Showman (2019) 1D model, where it is stronger by at least a factor of 10.
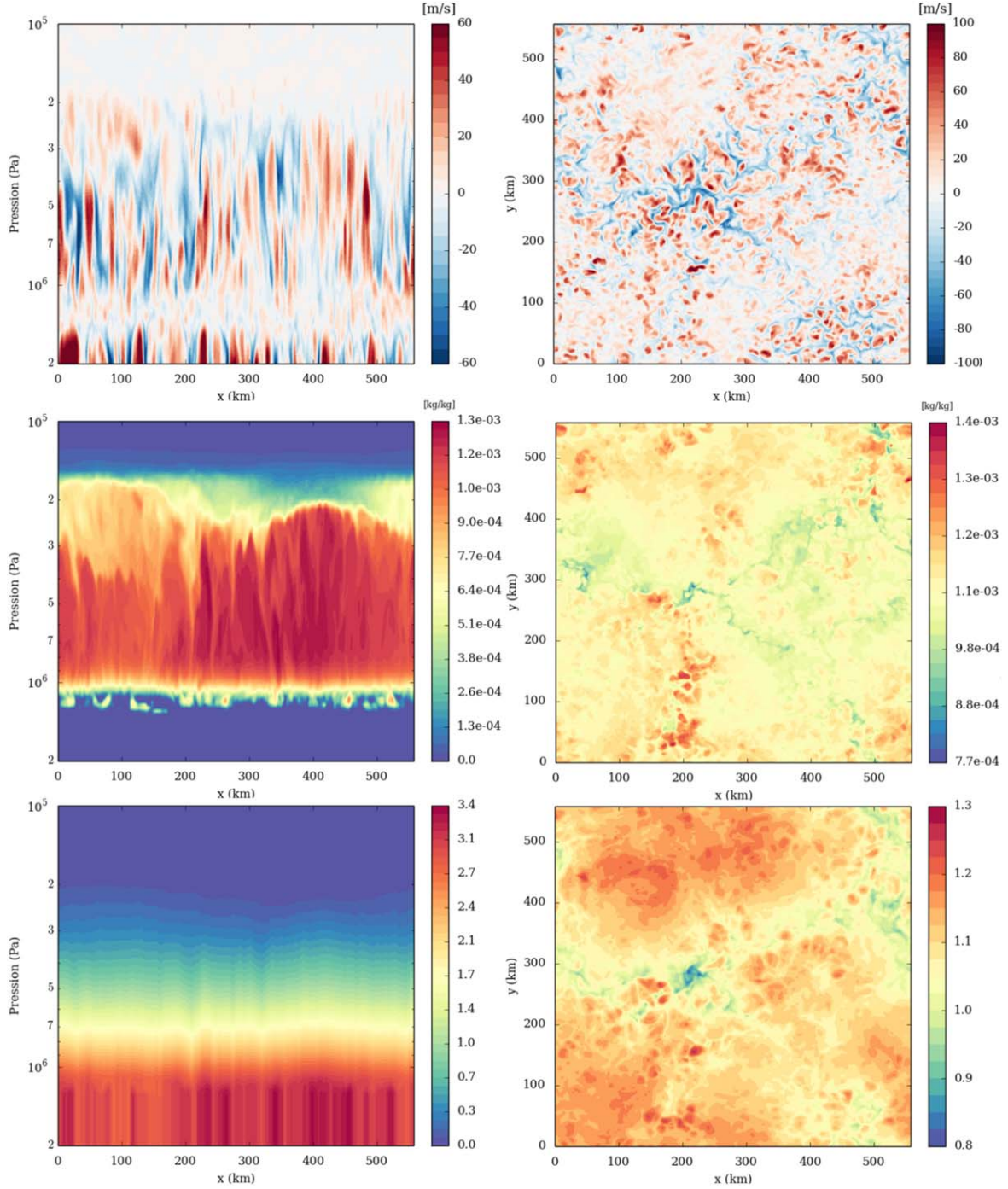
Figure 10. Snapshots of the vertical cross section (left column) and horizontal cross section at 5.4×10^5 Pa (right column) of the vertical wind (top row), cloud-mixing ratio (middle row), and cloud opacity (bottom row) for the 4000 K case with $MgSiO_3$ clouds and cloud particle number per dry airmass of 10^8 kg^{-1}.

4.2. Fe and Al_2O_3 Clouds

In Figure 6, the impact of Fe and Al_2O_3 on the convective layer depth is lower than that of $MgSiO_3$ clouds but is still noticeable. Figure 12 shows on the left column the domain-averaged vertical profiles of the potential temperature and IR heating rates for the 4000 K temperature case with Fe (top) and Al_2O_3 (bottom) clouds and six different particle number per dry airmass values. The associated domain-averaged vertical profiles of the reference particle radius, scattering albedo, and opacity are visible in Figure 23. As for $MgSiO_3$, the particle

number plays a role. The bigger particles, i.e., the 10^5 and 10^6 kg^{-1} cloud particle number density cases, barely affect the convective layer. The four other cases have different effects depending on the cloud particle species. For Fe clouds, the 10^9 kg^{-1} case will engender the strongest increase of the convective layer depth due to the higher scattering albedo and opacity. However, for Al_2O_3, the value of the particle number per dry airmass for which the convective depth is maximum is 10^8 kg^{-1}. The reference radius of these two cases is about 1 μm.
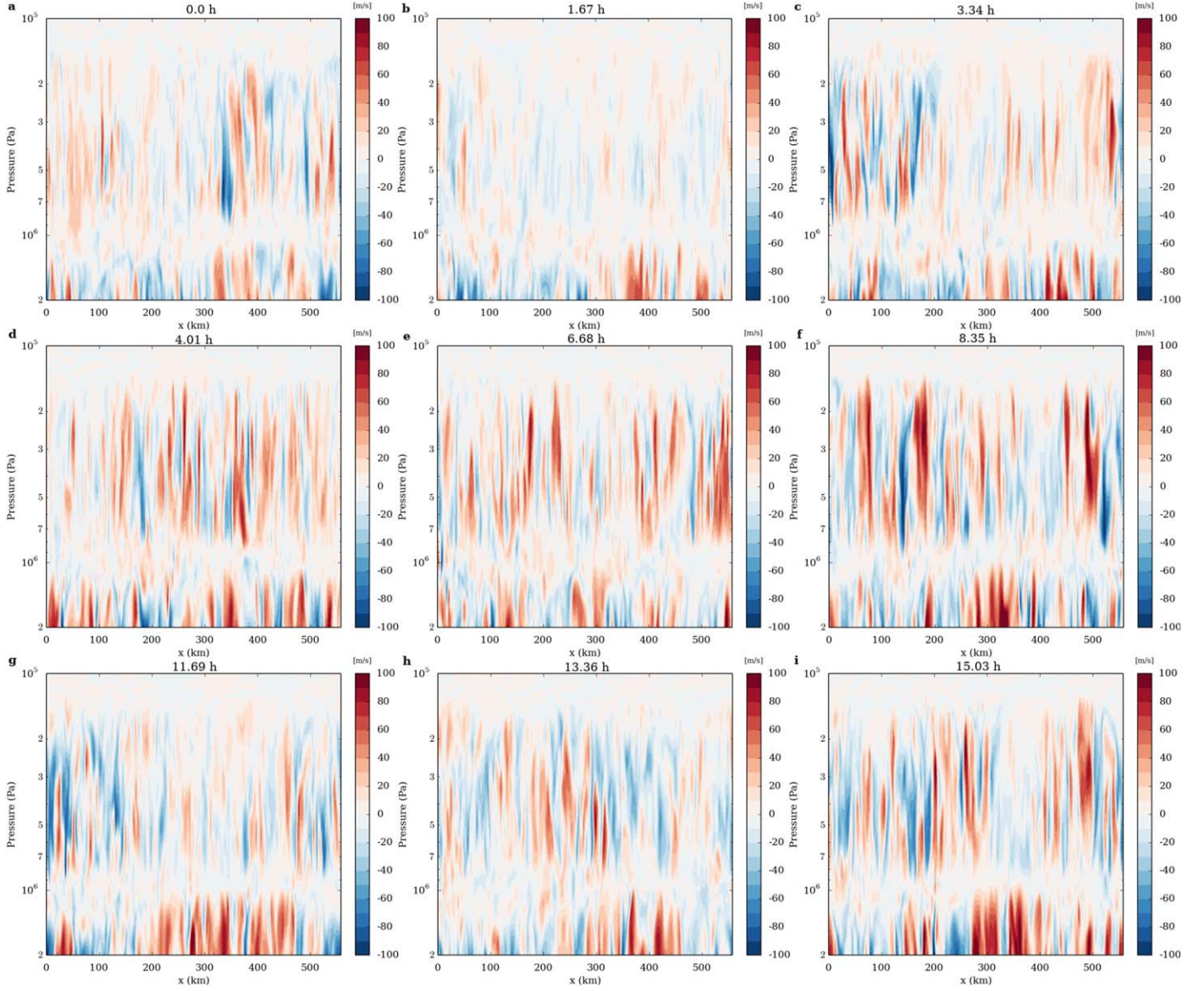
Figure 11. Time series of vertical cross sections of the vertical wind for the 4000 K case with MgSiO$_3$ clouds and cloud particle number per dry airmass of 10^8 kg^{-1}. The frequency between the panels is 1.67 hr.

4.3. CaTiO$_3$, Cr, and MnS Clouds

In Figure 6, the CaTiO$_3$, Cr and MnS clouds showed hardly any impact on the convective layer depth. Figure 13 shows the domain-averaged cloud-mixing ratio and scattering albedo vertical profiles for the three cloud species. The very small impact of the CaTiO$_3$, Cr, and MnS clouds are due to two factors, the mixing ratio and the vertical thickness of the cloud layer. The deep mixing ratio value for Ca, Cr, and Mn is 8.6 $\times 10^{-6}$, 1.76×10^{-5}, and 2.1 10^{-5}, between a factor of 10 and 100 lower than that of Al, where Al$_2$O$_3$ has a small impact. CaTiO$_3$ clouds have a similar depth than Al$_2$O$_3$ clouds; however, Cr and especially MnS will have a cloud layer that is significantly thinner. For MnS, the cloud layer will be present only at the very top of the convective layer and the mixing will be therefore less efficient compared to the other cloud compositions considered here. These two factors will lead to low opacity and low scattering albedo (meaning an increase in the outgoing infrared radiation compared to others clouds) and an overall limited impact on the convection depth.

4.4. Impact of Cloud Metallicity

Figure 5 showed the impact of the metallicity of the background atmosphere, and in this section the impact of the metallicity of the deep mixing ratio $q_{\rm deep}$ discussed in Section 2.3 is presented. Figure 14 shows the potential temperature for three temperature cases considered with MgSiO$_3$ and 10 times the solar metallicity. Compared to Figure 7, there is an increased number of detached convective layers with metallicity. For the 3000 K case, the increase in the convection layer height is larger with an increase in metallicity. There is also the formation of two detached convective layers for particle numbers per dry airmass of 10^7 and 10^8 kg^{-1}, though it is hardly discernible in the figure. There are three detached convective layers for the 4000 K case and four for the 5000 K. The height of these detached layers also vary. For the 5000 K case, the detached layer can start as high as 7×10^4 Pa. A convective layer at this altitude could affect species condensing at lower temperatures, such as Na$_2$S, ZnS, or KCl.
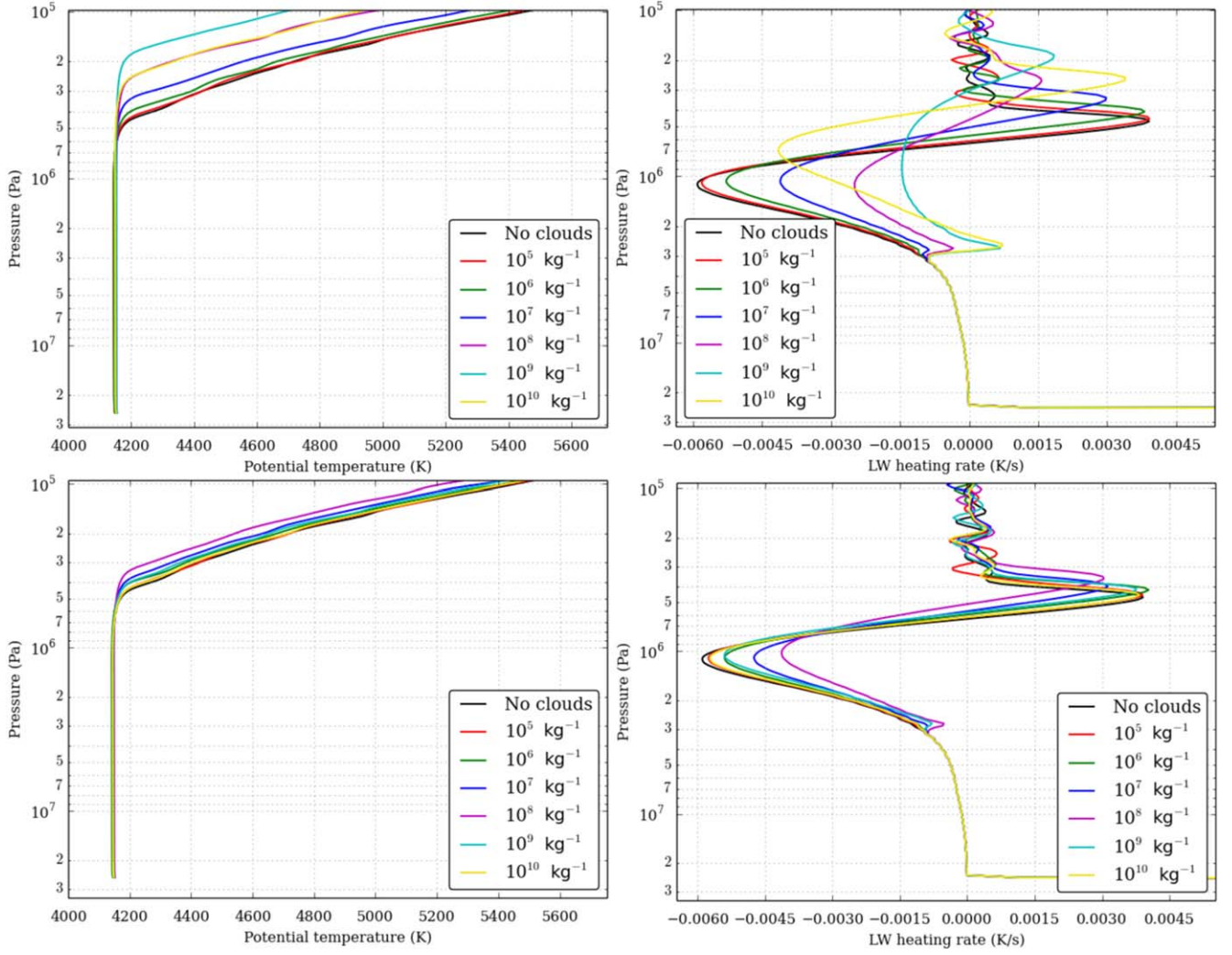
Figure 12. Domain-averaged vertical profiles of the potential temperature (left) and IR heating rates (right) for the 4000 K case with Fe (top row) and Al_2O_3 (bottom row) clouds and particle number per dry airmass between 10^5 and 10^{10} kg^{-1}.
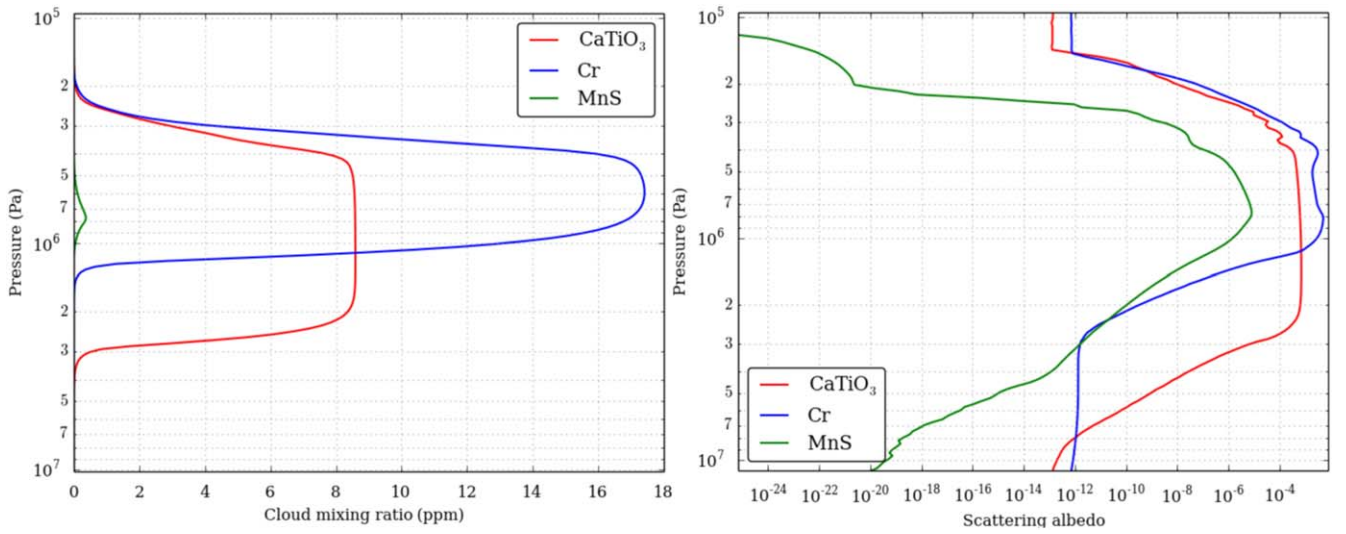

Figure 13. Domain-averaged vertical profiles of the cloud particle mixing ratio (left) and scattering albedo (right) for the 4000 K case with $CaTiO_3$, Cr, and MnS clouds and particle number per dry airmass of 10^8 kg^{-1}.
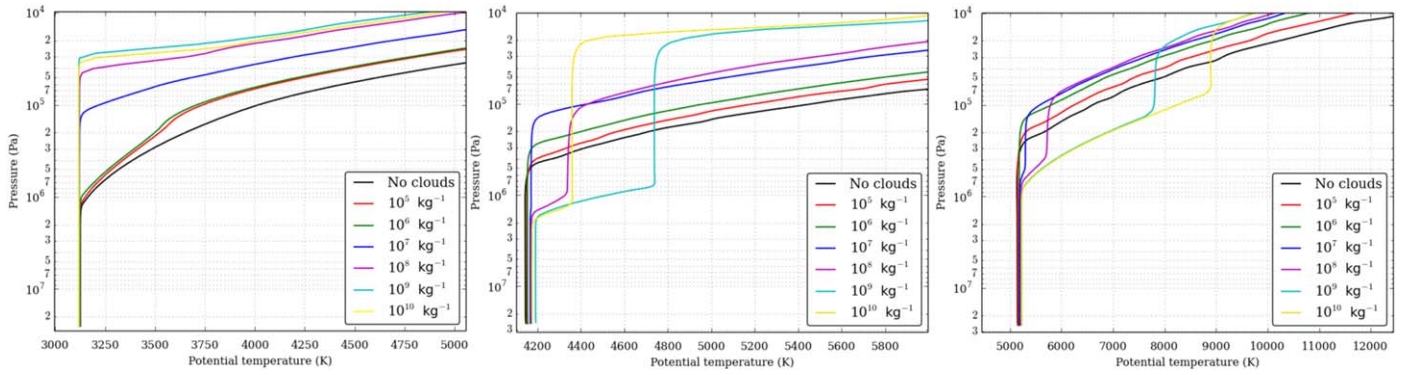
Figure 14. Domain-averaged vertical profiles of the potential temperature for the 3000 K (left), 4000 K (middle), and 5000 K (right) cases with $MgSiO_3$ clouds and particle number per dry airmass between 10^5 and 10^{10} kg^{-1} with solar metallicity multiplied by 10.

With a metallicity 10 times superior, Fe clouds with particle number densities of 10^9 and 10^{10} kg^{-1} will trigger a detached convective layer for the 5000 K case. On the other hand, the increase in metallicity for Al_2O_3 clouds does not trigger detached convective layers.

For the $CaTiO_3$, Cr, and MnS clouds, an increase in the metallicity by a factor of 10 is far too small for these three cloud compositions to have a significant impact. An increase of 100 will get a cloud opacity greater than 1 for $CaTiO_3$ and Cr.

5. Effect on the Emission Spectra

We produce emission spectra of our model output using the 3D multiple-scattering Monte Carlo radiative-transfer code GCMCRT (Lee et al. 2021). One-dimensional averaged vertical profiles of the temperature, pressure, and cloud properties across the simulation domain are produced for processing by GCMCRT. For chemical abundances, we assume chemical equilibrium and interpolate to a 2D table of the temperature and pressure of the species Volume Mixing Ratio (VMR) produced using the GGCHEM code (Woitke et al. 2018), assuming solar-metallicity elemental ratios from Asplund et al. (2009). These chemical abundance profiles are then used by GCMCRT to produce the opacity structure of the atmosphere. GCMCRT uses correlated-k tables for the gas opacity calculation; we produce $k$tables consisting of 512 wavelength points between 0.3 and 30 μm ($R \approx 100$), suitable for the resolution of the JWSTf NIRSPEC and MIRI instruments. K tables are produced using cross sections calculated using the HELIOS-K opacity code (Grimm & Heng 2015; Grimm et al. 2021), using the following line lists for different species: Na, K (Kurucz & Bell 1995), H_2O (Polyansky et al. 2018), CH_4 (Hargreaves et al. 2020), CO (Li et al. 2015), CO_2 (Yurchenko et al. 2020), and NH_3 (Coles et al. 2019). K coefficients in each band are weighted by the local VMR of spectrally active species using the random overlap method (e.g., Amundsen et al. 2017). GCMCRT also calculates the contribution from H_2, He, and H CIA pairs (Karman et al. 2019) and Rayleigh scattering opacity sources. For the cloud opacity calculations, we assume the same size distribution as used in the simulations, as well as the same MieX code (Wolf & Voshchinnikov 2004) and optical constants (Kitzmann & Heng 2018).

Figure 15 shows the emission spectra for the six cloud compositions considered with a cloud particle density of 10^8 kg^{-1} for the 4000 K case, corresponding to Figure 6. As expected, the species that have the most impact on the flux are the one with the most impact on the deep convection, i.e.,

$MgSiO_3$, Fe, and Al_2O_3. However, there is a several orders of magnitude decrease in flux for each species, especially below 0.5 μm and between 1 and 2 μm. For the first one, the spectral features are flattened by the clouds, and for the second one the spectral features are flattened by some clouds, but there is also the generation of other spectral features. Above 6 μm there is no significant difference between the clear-sky and cloudy cases. The larger impact of the clouds is in the optical, whereas the brown dwarfs are preferably observed in the IR due to the low magnitude in the optical.

Figure 16 shows the thermal flux spectra with $MgSiO_3$ cloud particle number density between 10^5 and 10^{10} kg^{-1} for the 3000, 4000, and 5000 K cases. For the 3000 K case, there are three groups: for 10^5 and 10^6 kg^{-1} the flux decrease is small, for 10^7 and 10^{10} kg^{-1} the flux decrease is moderate, and for 10^8 and 10^9 kg^{-1} the flux decrease is strong, all linked to the convective layer depth. The smoothing of the spectral features is strong for the 10^8 and 10^9 kg^{-1} cases, with a new spectral feature between 4 and 5 μm. The trend in particle number density is similar for the two other temperature cases—the deeper the convective layer is the lower the thermal flux is. The smoothing of the spectral features below 0.5 μm is stronger with temperature, as for the spectral features between 1 and 2 μm.

Figure 17 shows the same plot as Figure 15 but for Fe and Al_2O_3 clouds for the 4000 K case. As shown in Figure 12, the impact of Fe on the height of the convective layer is stronger than the one of Al_2O_3, and therefore, the decrease in the thermal amplitude is stronger for Fe clouds. The cloud particle number density cases for which the increase of the convection depth is stronger, 10^9 for Fe and 10^{10} kg^{-1} for Al_2O_3, have the strongest thermal flux decrease.

Figure 18 shows the magnitude–color diagram in the J and Kbands for the clear sky and the different clouds considered compared to observed brown dwarfs (Dupuy & Liu 2012). As expected, there is a strong effect of the clouds, with the clear-sky points (circle) being bluer than the cloudy cases. Colors of the coldest modeled temperatures are consistent with some observed T dwarfs. The cloud cases have a Jmagnitude consistent with observed T dwarfs, but with a much redder $J - K$ color. There is a strong effect of the cloud particle number density, shown here with 10^5 (empty symbols) and 10^8 kg^{-1} (filled symbols). As shown in Section 4.1, a low value of the particle number density will engender substantial cloud holes and the $J - K$ color will be bluer. The 10^8 kg^{-1} cases for $MgSiO_3$ exhibit a very high $J - K$ color, indicating that this
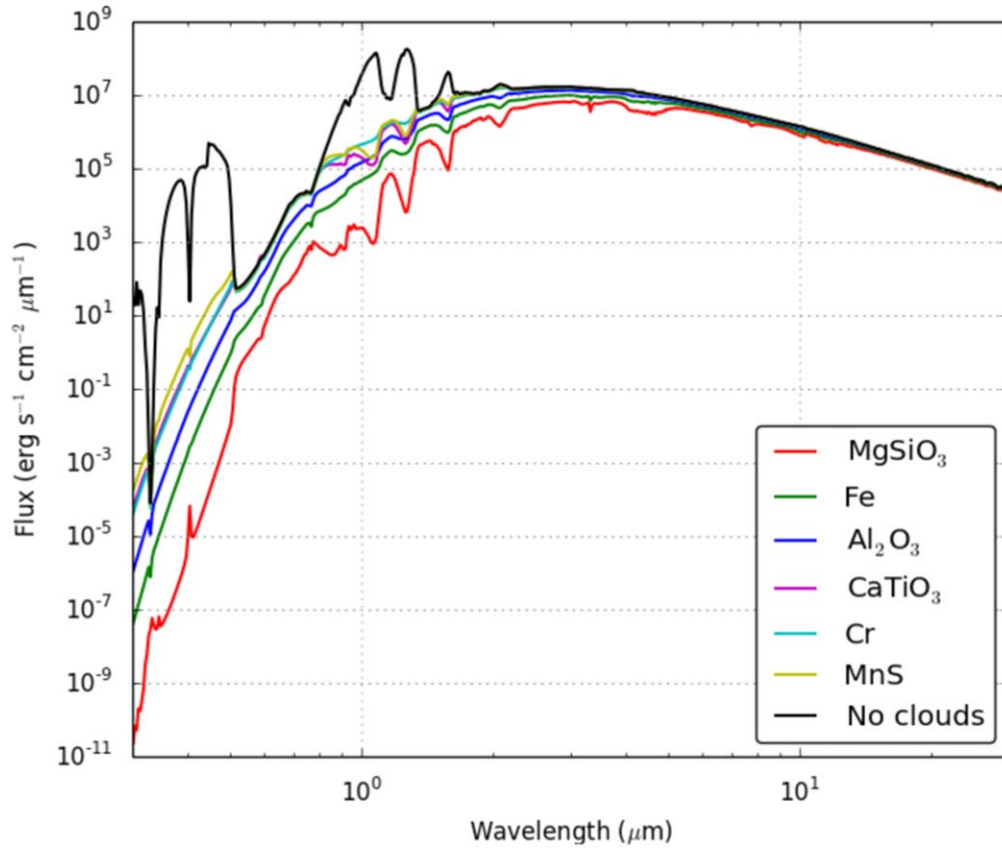
Figure 15. Thermal flux spectra for the six cloud compositions considered with a cloud particle number density of $10^8 \, \mathrm{kg}^{-1}$ for the 4000 K case.
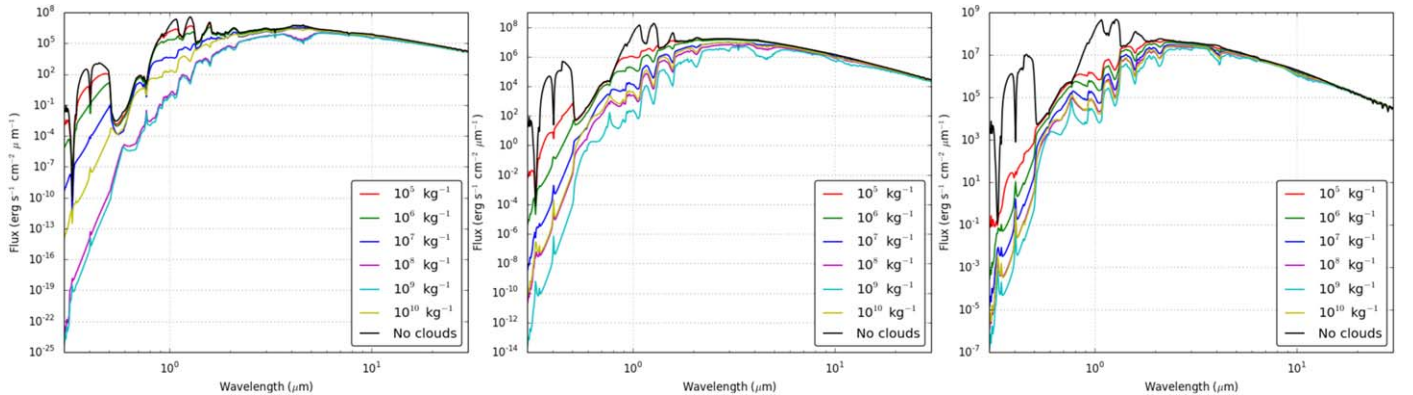

Figure 16. Thermal flux spectra with $MgSiO_3$ for the 3000, 4000, and 5000 K case and cloud particle number density between 10^5 and $10^{10} \, \mathrm{kg}^{-1}$.

value may not be realistic as it leads to a cloud deck that is too thick and homogeneous. These simulations are performed with solar metallicity; higher metallicity will increase the depth of the convective layer and therefore the $J - K$ color would be redder, but on the other hand, with a lower metallicity, the $J - K$ color will appear bluer and closer to the observations. Our model does not represent large-scale features of the general circulation that could modulate cloudiness through large-scale uplift or subsidence.

6. Conclusion

The model presented here is the first 3D convection-resolving model to model the radiative impact of the different types of clouds in brown dwarf atmospheres.

Without clouds, the convection depth increases with temperature, leading to larger convective cells and stronger vertical wind amplitude, reaching 600 m s^{-1} for the most extreme case. The vertical eddy diffusion from the resolved convection also increases with temperature, with values higher but consistent with previous estimations from the convection-resolving model and consistent with previous mixing-length theory estimations.

Several cloud compositions were tested with this model. The silicate clouds with $MgSiO_3$ are the ones with the most impact. The depth of the convective region is increased by heating at the cloud base, and for a particle radius around 1 μm, this heating is so strong that it destabilizes the atmosphere, leading to an independent detached cloud layer. The detached cloud is present for a larger particle radius range as the temperature increases. The temporal frequency is of similar order to the Tan
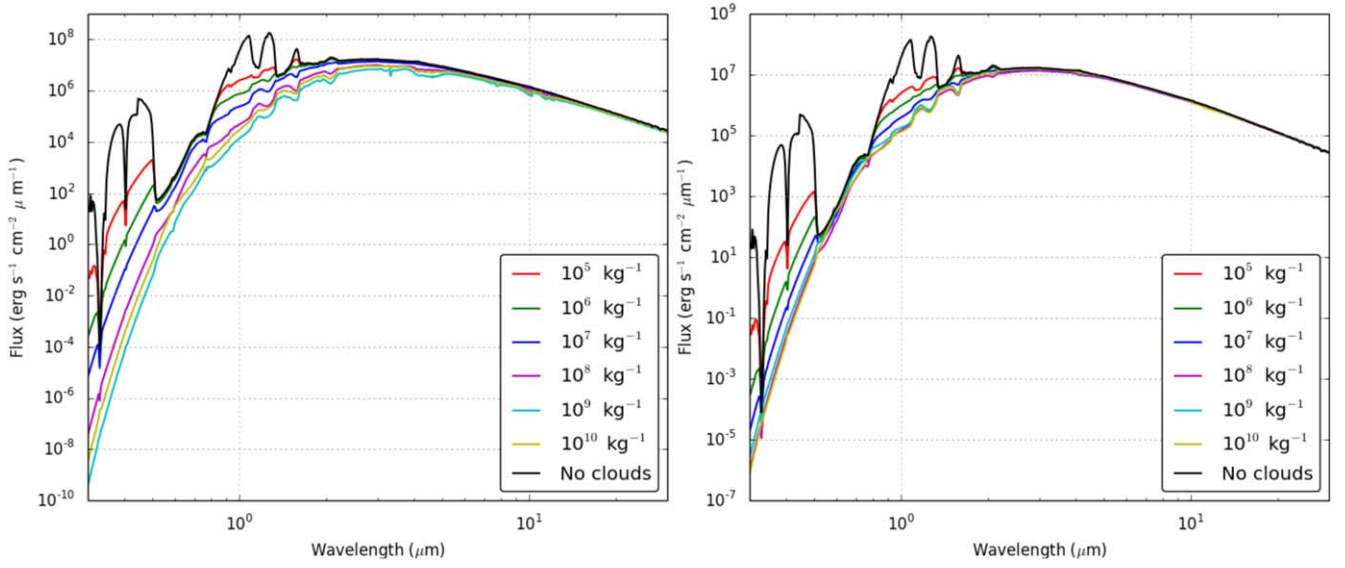
Figure 17. Thermal flux spectra with Fe and Al_2O_3 for the 4000 K case and cloud particle number density between 10^5 and 10^{10} kg^{-1}.
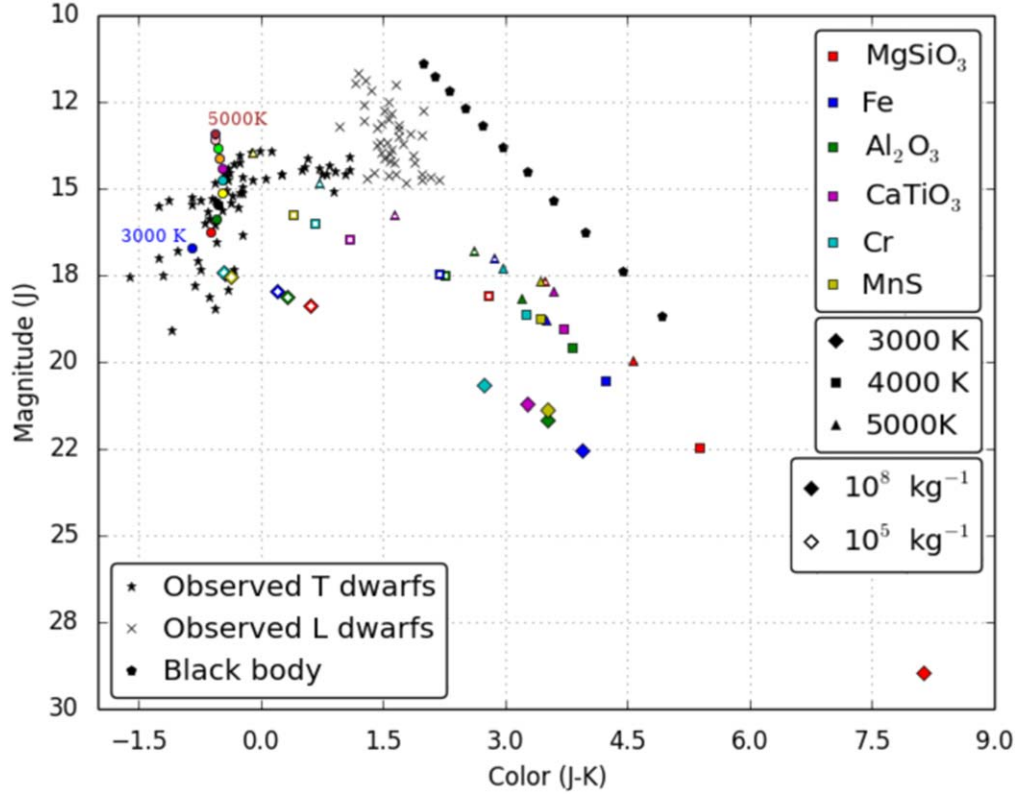

Figure 18. Magnitude–color diagram in the J and K bands for the clear-sky cases (circle; see Figure 1 for color bar) and the six cloud species considered (see Figure 6 for the color bar) for three temperatures and two cloud particle number densities, 10^5 (empty symbols) and 10^8 kg^{-1} (filled symbols), compared to observed brown dwarfs (Dupuy & Liu 2012).

& Showman (2019) 1D model; however, the domain-mean variability is significantly weaker.

The cloud particle number per dry airmass has a significant impact on the presence of cloud holes. For values above 10^7 kg^{-1}, there is a complete cloud coverage. For values below it, there is a significant presence of cloud holes. The temperature also has an impact on the presence of cloud holes; at low temperatures, the clouds are puffier, whereas at higher

temperatures, there is an aggregation of clouds due to the size of the convective cells.

The Fe and Al_2O_3 clouds also have a significant impact on the deep convective layer depth, but the heating at the cloud base is not strong enough to engender a detached cloud-convective layer.

However, cloud particles of $CaTiO_3$, Cr, and MnS have limited impact on the convection depth and therefore on the

emission spectra, due to the low abundance of condensable gas and the thin layer where the cloud condenses.

Two metallicities have been used in this study, solar metallicity and 10 times the solar metallicity. The depth of the clear-sky convective layer is slightly deeper, with an increased metallicity. The depth of the detached cloud-convective layer is more affected, with a significant increase.

The different cloud composition affects more or less the convection depth and the thermal structure above and therefore impacts the thermal spectra. There is a decrease in the flux amplitude and a smoothing of the spectra due to the clouds. MgSiO$_3$ clouds have the most impact on the emission spectra. The effect of σ (the nondimensionalized constant measuring the width of the particle size distribution) on the cloud deck was not studied; however, it could have a significant effect on the effective radius and therefore on the radiative properties of the clouds.

This cloud-convective feedback could also be present in hot giant exoplanets; the insolation and the specific star spectra could have a strong effect on the cloud layer. The insolation could bring extra heat and destabilize the atmosphere as on Earth or, on the contrary, stabilize a region like Venus' deep clouds (Imamura et al. 2014; Lefèvre et al. 2018). Different spectra could have an impact on the energy deposition in the atmosphere, as for Proxima Centauri b (Lefèvre et al. 2021). In hot Jupiter cloud studies, the moment formalism is sometimes used in microphysical modeling (Lee et al. 2016; Lines et al. 2018), allowing the particle number density to be then determined, as well as the different particle size distributions (Christie et al. 2021).

Charnay et al. (2018) showed a strong gravity effect on the chemistry and microphysics and the overall color. A similar study needs to be conducted with both higher and lower gravity to capture its impact on the cloud deck altitude and depth.

A nongray radiative-transfer scheme would be beneficial to fully understand the radiative effects of the different cloud compositions, with the correlated-k formalism, for example. The feedback due to specific absorption/emission lines, with a spectral dependence of the extinction and scattering coefficients for the different cloud species, could be therefore quantified.

In this study, no wind shear was imposed on the domain, and the depth of the deep convective layer is governed by the IR heating of the deep atmosphere. However, the dynamics and global atmospheric circulation will impose wind shear that could affect convection as well as gravity-wave generation and vertical propagation (Frits & Alexander 2003). Such gravity waves could impact the condensation and nucleation of species condensing at higher altitudes (Parent et al. 2020).

The heat capacity of H/He is set constant in the model, while the temperature varies by several thousands of Kelvin over the vertical. In such a temperature range, the heat capacity variation should be taken into account in future work as it could impact the stability in parts of the atmosphere.

The condensation process in our model is highly simplified, with silicate vapor, for example, condensing into enstatite; this is an approximation, and a chemical model is therefore needed to resolve the complexity of such environments. Such improvement will permit the simultaneous presence of multiple cloud types and the interaction between the different kinds of clouds.

The microphysical scheme used in this study is idealized, coagulation and growth of cloud particles are not taken into account, and effects of nonspherical particles and microporosity (Samra et al. 2020) and resolving the cloud particle size distribution (e.g., Gao et al. 2018) are not implemented. The latent heat release of different clouds is overlooked in the study, and an implementation of such energy release could help the study of local storms (Tan & Showman 2017).

Convective-resolving studies have been used for Earth (Rio et al. 2010) and Mars (Colaïtis et al. 2013) atmospheres to improve the parameterization of the convection in the GCMs. The present study could be the starting point of such methodology for brown dwarfs and hot giant exoplanets.

Appendix A
Rosseland Mean

Figure 19 shows the Rosseland mean extinction coefficient for the six cloud species over the temperature and particle radius ranges considered. The extinction coefficients have a similar structure for all the species, with a value below 1 for radii below 1 μm and a value above 1 for radii above 1 μm. The transition radius varies with the species and temperature. MgSiO$_3$ particles have the highest transition radius, whereas Cr particles have the lowest. Cr and Fe particles have a temperature dependence of the extinction coefficient between 1 and 10 μm, where the coefficient is stronger at high temperatures.

Figure 20 shows the Rosseland mean single-scatter coefficient for the six cloud species considered over the temperature and particle radius ranges. The scattering coefficients have a similar structure for all the species, with a value below 1 for radii below 1 μm and a value above 1 for radii above 1 μm. The transition radius varies with the species and temperature. MgSiO$_3$ particles have the highest transition radius, whereas Cr particles have the lowest. Contrary to the extinction coefficient, all the species have a temperature dependence for radius above 1 μm. Al$_2$O$_3$, Cr, Fe, and MnS have a stronger coefficient for lower temperature whereas for CaTiO$_3$ and MgSiO$_3$ it is the opposite.

Figure 21 shows the Rosseland mean asymmetry factor for the six cloud species over the temperature and particle radius ranges considered. Contrary to the extinction and scattering coefficients, there is a broad range of values and radius dependency for the asymmetry factor. Al2O3 and MgSiO3 particles have values above 0.1 above a radius of 1 μm, with a drop in radius close to 100 μm. Cr and Fe particles have an asymmetry factor varying from 10^{-12} for radius 1 μm and below to 1 for a 100 μm radius at high temperature. CaTiO3 particles have an asymmetry factor varying from 10^{-7} for the lowest radius to 0.3 for the highest, with a strong drop in radius around 100 μm. MnS has an asymmetry factor between 10^{-3} and 10^{-2} for all the radius ranges, with a strong drop in radius between 1 and 10 μm.
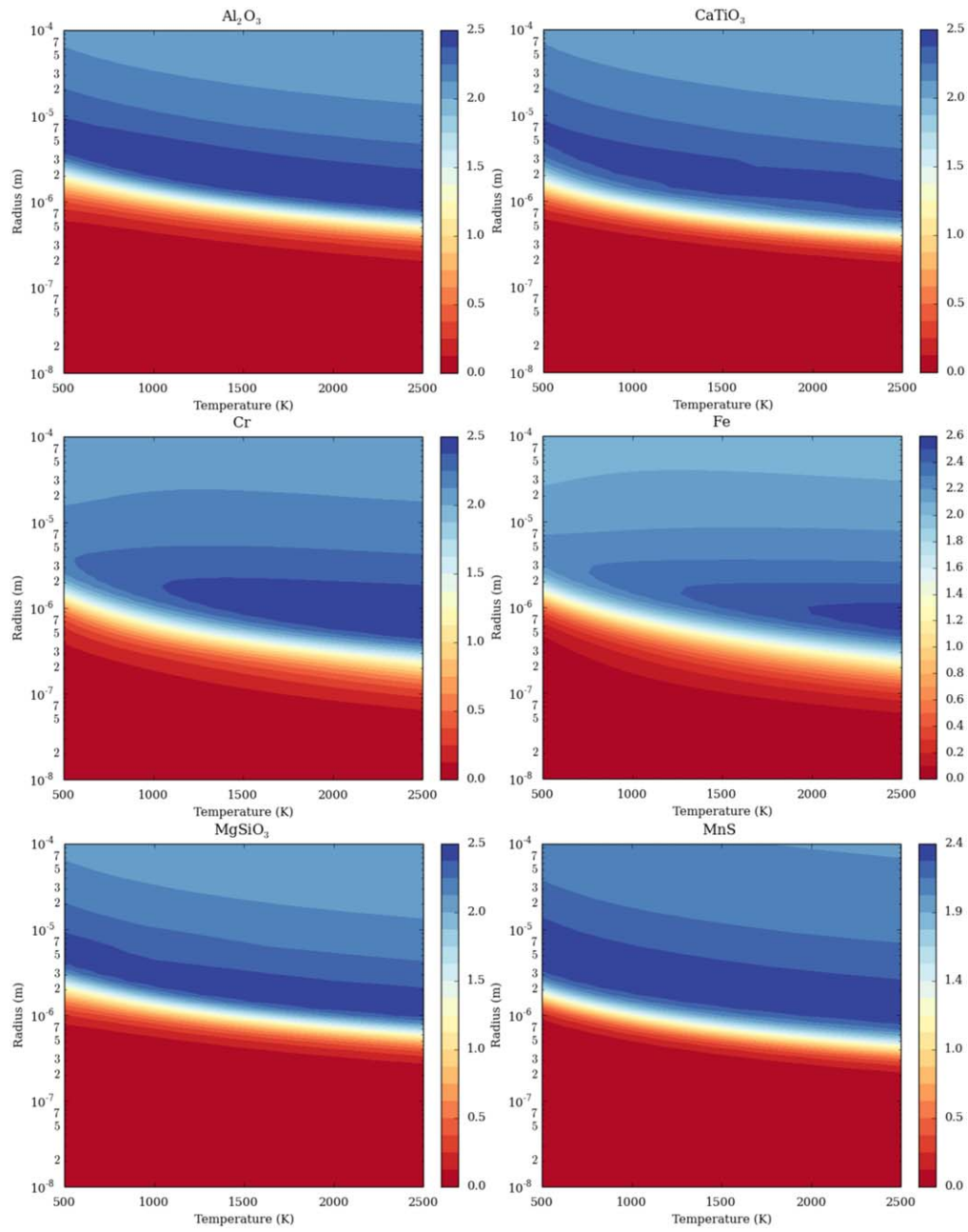
Figure 19. Rosseland mean extinction coefficient Q_{ext} for the Al_2O_3, $CaTiO_3$, Cr, Fe, $MgSiO_3$, and MnS clouds.
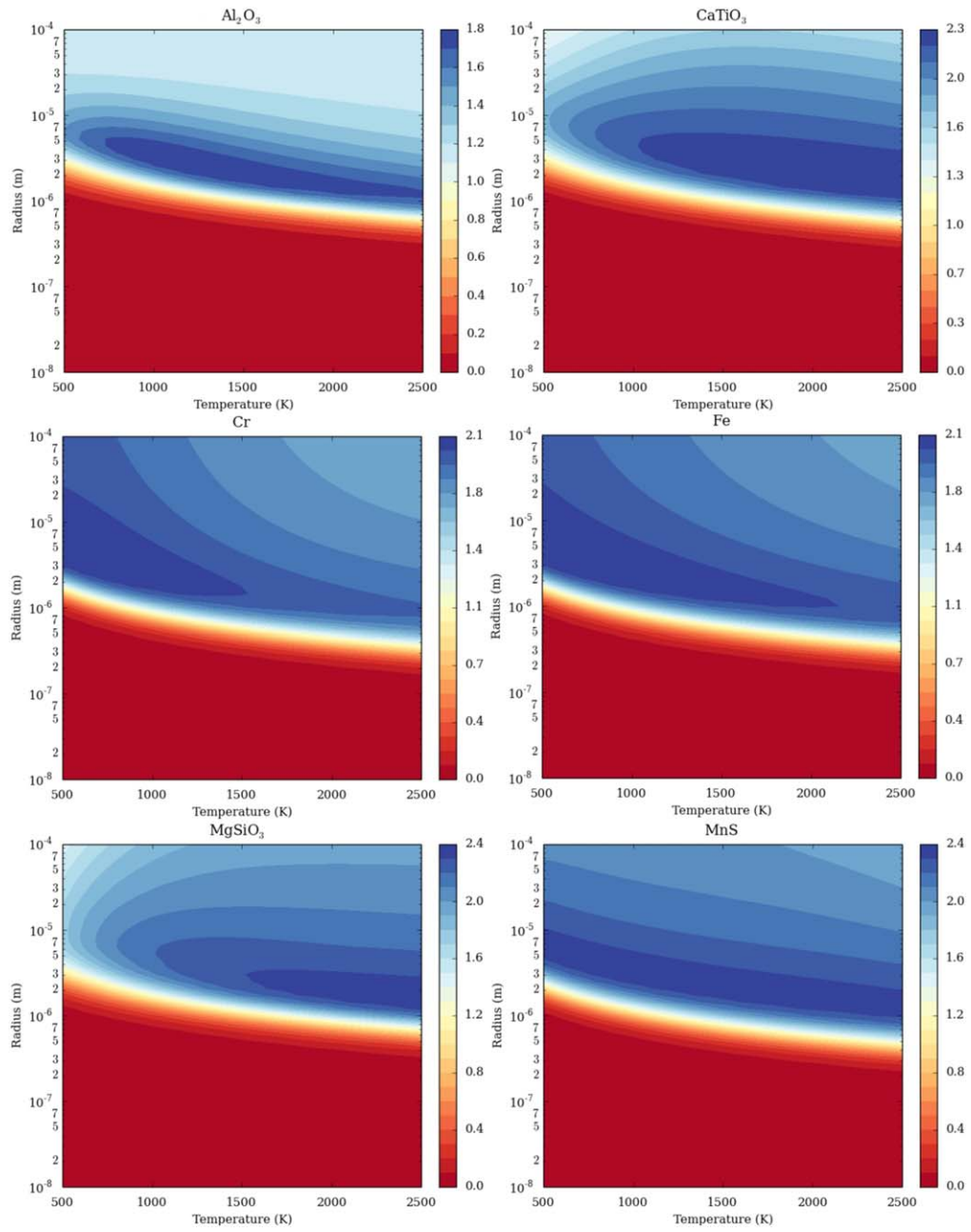
Figure 20. Rosseland mean single-scatter coefficient Q_{scat} for the Al_2O_3, $CaTiO_3$, Cr, Fe, $MgSiO_3$, and MnS clouds.
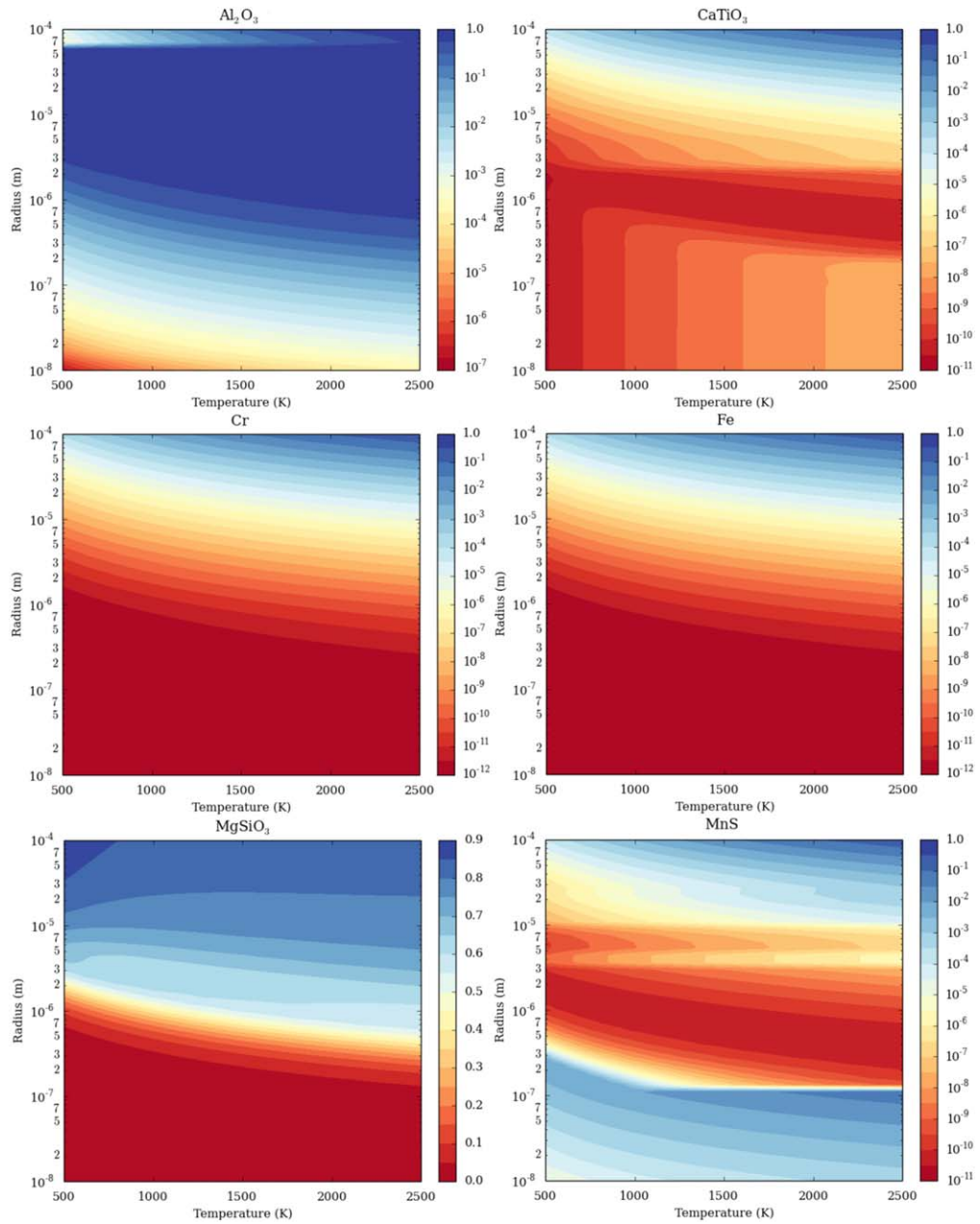
Figure 21. Rosseland mean asymmetry factor for the Al_2O_3, $CaTiO_3$, Cr, Fe, $MgSiO_3$, and MnS clouds.

Appendix B
MgSiO₃ Clouds

Figure 22 shows the domain-averaged vertical profiles of the reference radius, scattering albedo, and cloud opacity for the 3000 K, 4000 K and 5000 K cases with MgSiO3 clouds for the 6 particle number per dry airmass cases.
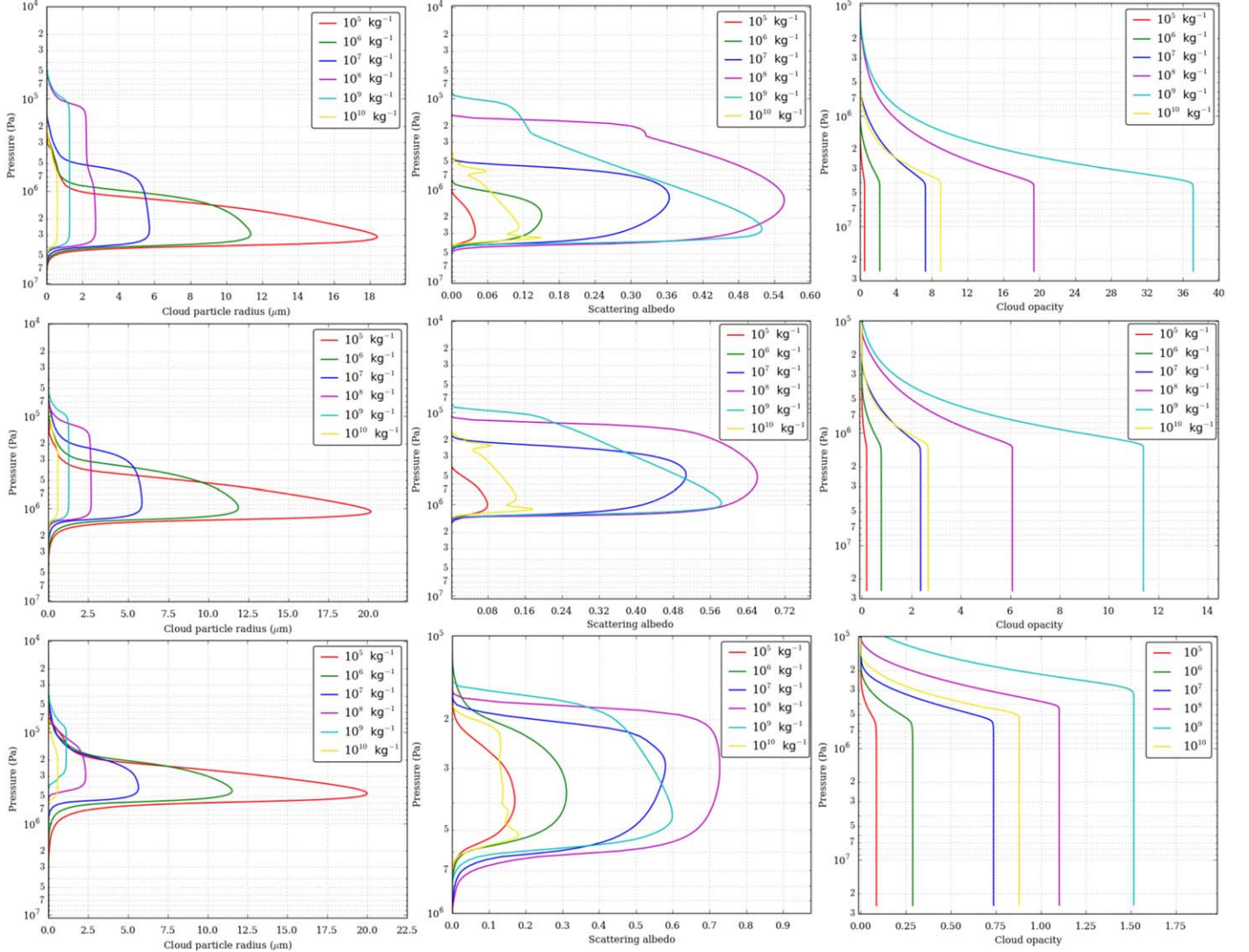
Figure 22. Domain-averaged vertical profiles of the reference radius (left column), scattering albedo (middle column), and cloud opacity (right column) for the 3000 K (top row), 4000 K (middle row) and 5000 K (bottom row) cases with MgSiO₃ clouds and particle number per dry airmass between 10^5 and 10^{10} kg^{-1}.

Appendix C
Fe and Al2O₃ Clouds

Figure 23 shows the domain-averaged vertical profiles of the reference radius, scattering albedo, and cloud opacity for the 4000 K case with Fe and Al2O3 clouds for the 6 particle number per dry airmass cases.
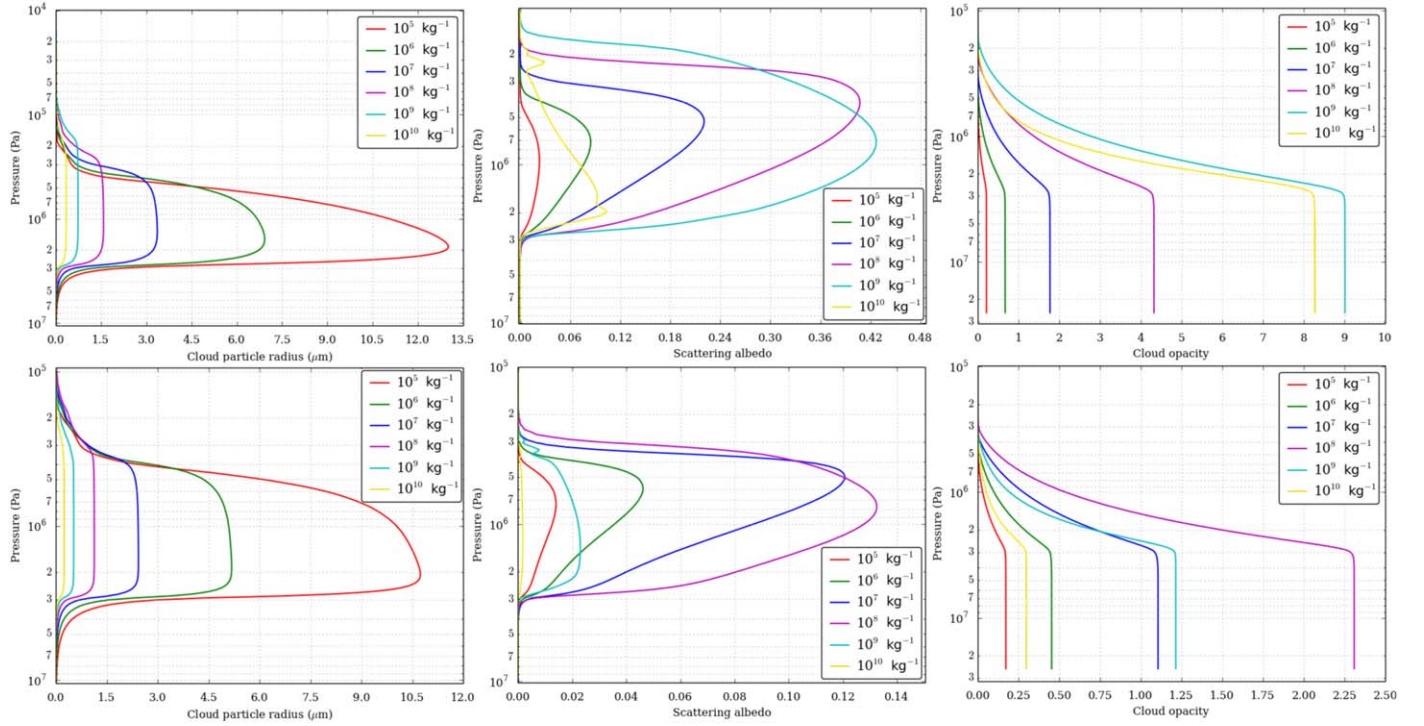
Figure 23. Domain-averaged vertical profiles of the reference radius (left column), scattering albedo (middle column), and cloud opacity (right column) for the 4000 K case with Fe (top row) and Al$_2$O$_3$ (bottom row) clouds and particle number per dry airmass between 10^5 and 10^{10} kg^{-1}.

ORCID iDs

Maxence Lefèvre ⬤ https://orcid.org/0000-0002-3143-9716
Xianyu Tan ⬤ https://orcid.org/0000-0003-2278-6932
Elspeth K. H. Lee ⬤ https://orcid.org/0000-0002-3052-7116
R. T. Pierrehumbert ⬤ https://orcid.org/0000-0002-5887-1197

References

Ackerman, A. S., & Marley, M. S. 2001, ApJ, 556, 872
Allard, F., Hauschildt, P. H., Alexander, D. R., Tamanai, A., & Schweitzer, A. 2001, ApJ, 556, 357
Allard, F., Homeier, D., Freytag, B., & Sharp, C. M. 2012, in Low-Mass Stars and the Transition Stars/Brown Dwarfs, ed. C. Reylé, C. Charbonnel, & M. Schultheis, Vol. 57 (Les Ulis: EDP Sciences), 3
Amundsen, D. S., Tremblin, P., Manners, J., Baraffe, I., & Mayne, N. J. 2017, A&A, 598, A97
Apai, D., Karalidi, T., Marley, M. S., et al. 2017, Sci, 357, 683
Apai, D., Radigan, J., Buenzli, E., et al. 2013, ApJ, 768, 121
Asplund, M., Grevesse, N., Sauval, A. J., & Scott, P. 2009, ARA&A, 47, 481
Barman, T. S., Macintosh, B., Konopacky, Q. M., & Marois, C. 2011, ApJL, 735, L39
Biller, B. A., Crossfield, I. J. M., Mancini, L., et al. 2013, ApJL, 778, L10
Bordwell, B., Brown, B. P., & Oishi, J. S. 2018, ApJ, 854, 8
Artigau, É, Bouchard, S., Doyon, R., & Lafrenière, D. 2009, ApJ, 701, 1534
Bryan, G. H., & Fritsch, J. M. 2002, MWRv, 130, 2917
Buenzli, E., Marley, M. S., Apai, D., et al. 2015, ApJ, 812, 163
Burrows, A., Sudarsky, D., & Hubeny, I. 2006, ApJ, 640, 1063
Chapman, S., & Cowling, T. G. 1970, The Mathematical Theory of Non-uniform Gases. An Account of the Kinetic Theory of Viscosity, Thermal Conduction and Diffusion in Gases (Cambridge: Cambridge Univ. Press)
Charnay, B., Bézard, B., Baudino, J. L., et al. 2018, ApJ, 854, 172
Christie, D. A., Mayne, N. J., Lines, S., et al. 2021, MNRAS, 506, 4500
Colaïtis, A., Spiga, A., Hourdin, F., et al. 2013, JGRE, 118, 1468
Coles, P. A., Yurchenko, S. N., & Tennyson, J. 2019, MNRAS, 490, 4638
Cushing, M. C. 2014, in 50 Years of Brown Dwarfs, ed. V. Joergens, Vol. 401 (Berlin: Springer), 113
Deardorff, J. W. 1980, BoLMe, 18, 495
Dupuy, T. J., & Liu, M. C. 2012, ApJS, 201, 19
Freedman, R. S., Lustig-Yaeger, J., Fortney, J. J., et al. 2014, ApJS, 214, 25
Freytag, B., Allard, F., Ludwig, H.-G., Homeier, D., & Steffen, M. 2010, A&A, 513, A19
Frits, D. C., & Alexander, M. J. 2003, RvGeo, 41, 1112
Gao, P., Marley, M. S., & Ackerman, A. S. 2018, ApJ, 855, 86
Gillon, M., Triaud, A. H. M. J., Jehin, E., et al. 2013, A&A, 555, L5
Grimm, S. L., & Heng, K. 2015, ApJ, 808, 182
Grimm, S. L., Malik, M., Kitzmann, D., et al. 2021, ApJS, 253, 30
Hargreaves, R. J., Gordon, I. E., Rey, M., et al. 2020, ApJS, 247, 55
Helling, C., Ackerman, A., Allard, F., et al. 2008, MNRAS, 391, 1854
Helling, C., & Casewell, S. 2014, A&ARv, 22, 80
Imamura, T., Higuchi, T., Maejima, Y., et al. 2014, Icar, 228, 181
Kang, S.-L., & Bryan, G. H. 2011, MWRv, 139, 2901
Karalidi, T., Apai, D., Marley, M. S., & Buenzli, E. 2016, ApJ, 825, 90
Karman, T., Gordon, I. E., van der Avoird, A., et al. 2019, Icar, 328, 160
Kirkpatrick, J. D. 2005, ARA&A, 43, 195
Kitzmann, D., & Heng, K. 2018, MNRAS, 475, 94
Kurucz, R. L., & Bell, B. 1995, Atomic Line List, Kurucz CD-ROM No. 23 (Cambridge, MA: Smithsonian Astrophysical Observatory)

Kylling, A., Stamnes, K., & Tsay, S. C. 1995, JAtC, 21, 115
Lee, E., Dobbs-Dixon, I., Helling, C., Bognar, K., & Woitke, P. 2016, A&A, 594, A48
Lee, E. K. H., Casewell, S. L., Chubb, K. L., et al. 2020, MNRAS, 496, 4674
Lee, E. K. H., Wardenier, J. P., Prinoth, B., et al. 2021, arXiv:2110.15640
Lefèvre, M., Lebonnois, S., & Spiga, A. 2018, JGRE, 123, 2773
Lefèvre, M., Turbet, M., & Pierrehumbert, R. 2021, ApJ, 913, 101
Lewis, N. K., Showman, A. P., Fortney, J. J., et al. 2010, ApJ, 720, 344
Li, G., Gordon, I. E., Rothman, L. S., et al. 2015, ApJS, 216, 15
Li, Z., & Wang, H. 2003, PhRvE, 68, 061206
Lines, S., Mayne, N. J., Boutle, I. A., et al. 2018, A&A, 615, A97
Lodders, K. 2003, ApJ, 591, 1220
Madhusudhan, N., Burrows, A., & Currie, T. 2011, ApJ, 737, 34
Markowski, P. M., & Bryan, G. H. 2016, MWRv, 144, 1841
Marley, M. S., Saumon, D., & Goldblatt, C. 2010, ApJL, 723, L117
Metchev, S. A., Heinze, A., Apai, D., et al. 2015, ApJ, 799, 154
Morley, C. V., Fortney, J. J., Marley, M. S., et al. 2012, ApJ, 756, 172
Morley, C. V., Marley, M. S., Fortney, J. J., et al. 2014, ApJ, 787, 78
Moses, J. I., Visscher, C., Fortney, J. J., et al. 2011, ApJ, 737, 15
Nakajima, T., Oppenheimer, B. R., Kulkarni, S. R., et al. 1995, Natur, 378, 463
Parent, A., Falconer, R. E., Lee, E. K. H., Meyer, K. A., & Stark, C. R. 2020, A&A, 635, A159
Pierrehumbert, R. T. 2010, Principles of Planetary Climate (Cambridge: Cambridge Univ. Press)
Polyansky, O. L., Kyuberis, A. A., Zobov, N. F., et al. 2018, MNRAS, 480, 2597
Pruppacher, H. R., & Klett, J. 1978, Microphysics of Clouds and Precipitation (Dordrecht: D. Reidel Publishing Company)
Radigan, J., Jayawardhana, R., Lafrenière, D., et al. 2012, ApJ, 750, 105
Rebolo, R., Martin, E. L., Basri, G., Marcy, G. W., & Zapatero-Osorio, M. R. 1996, ApJL, 469, L53
Rio, C., Hourdin, F., Couvreux, F., & Jam, A. 2010, BoLMe, 135, 469
Rosner, D. E. 1986, Transport Processes in Chemically Reacting Flow Systems (Amsterdam: Elsevier)
Samra, D., Helling, C., & Min, M. 2020, A&A, 639, A107
Shi, X., Hagen, H. L., Chow, F. K., Bryan, G. H., & Street, R. L. 2018, JAtS, 75, 611
Showman, A. P., & Kaspi, Y. 2013, ApJ, 776, 85
Showman, A. P., Tan, X., & Zhang, X. 2019, ApJ, 883, 4
Stevenson, D. J. 1979, GApFD, 12, 139
Stiel, L. I., & Thodos, G. 1963, Ind. Eng. Chem. Fundamen., 2, 233
Tan, X., Lefèvre, M., & Pierrehumbert, R. T. 2021, ApJL, 923, L15
Tan, X., & Showman, A. P. 2017, ApJ, 835, 186
Tan, X., & Showman, A. P. 2019, ApJ, 874, 111
Tan, X., & Showman, A. P. 2020, ApJ, 902, 27
Tan, X., & Showman, A. P. 2021a, MNRAS, 502, 678
Tan, X., & Showman, A. P. 2021b, MNRAS, 502, 2198
Tremblin, P., Bloch, H., González, M., et al. 2021, A&A, 653, A30
Tsuji, T. 2002, ApJ, 575, 264
Tsuji, T., Ohnaka, K., & Aoki, W. 1996, A&A, 305, L1
Visscher, C., Lodders, K., & Fegley, B. J. 2010, ApJ, 716, 1060
Wakeford, H. R., Visscher, C., Lewis, N. K., et al. 2017, MNRAS, 464, 4247
Wang, W. 2014, BoLMe, 151, 239
Witte, S., Helling, C., & Hauschildt, P. H. 2009, A&A, 506, 1367
Woitke, P., Helling, C., Hunter, G. H., et al. 2018, A&A, 614, A1
Wolf, S., & Voshchinnikov, N. V. 2004, CoPhC, 162, 113
Yurchenko, S. N., Mellor, T. M., Freedman, R. S., & Tennyson, J. 2020, MNRAS, 496, 5282
Zhang, X. 2020, RAA, 20, 099
Zhang, X., & Ahowman, A. P. 2014, ApJL, 788, L6